Title
Study of Zero and Finite Temperature Response of Discrete Deformable Surfaces

Author
Singh, Amit Rajnarayan

Publication Date
2018

Peer reviewed|Thesis/dissertation

UNIVERSITY OF CALIFORNIA

Los Angeles

Study of Zero and Finite Temperature Response of Discrete Deformable Surfaces

A dissertation submitted in partial satisfaction
of the requirements for the degree
Doctor of Philosophy in Mechanical Engineering

by

Amit Rajnarayan Singh

2018

ABSTRACT OF THE DISSERTATION

Study of Zero and Finite Temperature Response
of Discrete Deformable Surfaces

by

Amit Rajnarayan Singh
Doctor of Philosophy in Mechanical Engineering
University of California, Los Angeles, 2018
Professor Jeffrey D. Eldredge, Chair

We report on the effect of discreteness on mechanical and thermal response of closed deformable shells inspired by capsids of biological viruses. Generally, these structures are analyzed using continuum elasticity theories. The ratio of the in-plane stretching and the bending energies of the shell, called as the Föppl von Kármán (FvK) number, is an important dimensionless number that characterizes the key features of these shells. Through two new models of shells, we replace the continuum description by their discrete counterparts in incremental steps. The first model is a hybrid discrete-continuum description. It shows the presence of competing symmetries at low FvK numbers which are not detected in the continuum model. The second model shows that the FvK number controls the thermal response of these shells. Shells can be melted only at low FvK numbers. At values of FvK higher than the buckling transition, increase in thermal fluctuations gives rise to a pressure that crumples the shell and precludes melting.

The dissertation of Amit Rajnarayan Singh is approved.

Lihua Jin

Ajit Mal

Robijn F. Bruinsma

Jeffrey D. Eldredge, Committee Chair

University of California, Los Angeles

2018

TABLE OF CONTENTS

LIST OF FIGURES

LIST OF TABLES

ACKNOWLEDGMENTS

I am grateful to all my teachers. I thank Professor William S. Klug for accepting me in his research group and setting me on the project which has eventually become my dissertation. I am grateful to Professor Ajit Mal, Professor Christopher Lynch, Dr. Vinay Goyal and Professor William Klug, once again, who taught me the graduate classes on elasticity and finite element theories that gave me the foundational skills on which this research is based. I especially acknowledge the guidance and supervision of Professor Robijn Bruinsma as the principal investigator of my projects. Without his patient instructions this inter-disciplinary work would have never been successful. I also thank Professor Joseph Rudnick for his inputs throughout the course of this research. Dr. Andrej Košmrlj was very helpful for discussions about Chapter 3. I am very thankful to Professor Eldredge for stepping in when we needed help the most. He has been a great support in ensuring that I finish the work that I started with his colleague and friend Professor Klug. I also thank him for the great classes I took with him, making Fluid Dynamics my minor field. My special thanks to Dr. Luigi Perotti who has been like a mentor to me during my time at UCLA. I thank him for the several hours he has spent discussing my research projects and spotting crucial mistakes in my computer programs! He helped me keep pace when I slowed down and kept prodding me to move through thick and thin. I also thank Sanjay Dharmavaram for the many great discussions on a wide variety of topics that we had. Aditya and Jordan deserve special mention for being wonderful colleagues and friends for the past five years. I thank them for all the coursework that we took together and also for the several friendly exchanges. I thank Professor Christopher Lynch, Dean Jayathi Murthy and the Graduate Division for the financial support they provided after the tragic incident. Without it I would have not been able to bring this work to fruition. I thank IDRE for providing Hoffman2 cluster for computer simulations reported in this work. I have used many great open source software tools during this work and I wish to thank all their authors for their splendid work. Chapter 2 has sections which have been reproduced from [SPB17] which has been co-authored by me, Dr. Luigi Perotti, Professor Bruinsma, Professor Rudnick and Professor Klug. I am very

grateful to my wife, Mona, for being a rock solid support during this endurance. At last, I am thankful to my parents for their inspiration and hard work all along.

VITA

2005–2009 B. E. (Mechanical Engineering), Birla Institute of Technology and Science, Pilani, India

2009–2010 Technical Consultant, JDA Software Inc., Bangalore, India

2010–2011 Software Engineer, NIL Labs, Gurgaon, India

2011–2013 M.E. (Mechanical Engineering)

2013–2014 Graduate Student, Department of Mechanical and Aerospace Engineering, UCLA

2015–Present PhD Candidate, Department of Mechanical and Aerospace Engineering, UCLA

PUBLICATIONS

Singh, A. R., Perotti, L. E., Bruinsma, R. F., Rudnick, J., & Klug, W. S. (2017). Ground state instabilities of protein shells are eliminated by bucking. *Soft Matter, 13* (44), 8300–8308

CHAPTER 1

Introduction

Simple viruses are organisms of submicroscopic scale that have genetic material (RNA or DNA) enclosed in a protective shell called the capsid [FER04]. Understanding structural properties of viruses has played an important role in advancing nanotechnology. Nanotechnology relies on different microscopic materials like iron oxide nanoparticles, liposomes, antibodies, dendrimers, nanoshells, quantum dots and viruses [KM10]. Viruses are useful for nanotechnologists because they form regular structures of homogeneous size. They are mechanically and chemically stable and easy to produce *in-vitro* by self-assembly. Besides, viruses have dynamic structural properties which can be modified by genetically or chemically manipulating their capsids. In the nature, viruses are found in a variety of shapes like helical, quasispherical, prolate, complex and enveloped. In this work, we will restrict our scope to quasispherical shapes. Quasispherical viruses can either be spherical or polyhedral as shown in Figure 1.1.

To study the mechanics of quasispherical viral shells we need a systematic description of their structure. The physical principles of construction of such structures were explained in a landmark paper by Caspar and Klug [CK62] which we discuss in the next section.

1.1 Caspar-Klug Construction

Crick and Watson [CW56] suggested that viruses have limited genetic material which can be used to produce only a few types of proteins. To use the limited genomic information efficiently, the shells of viruses must be made up of identical *subunits*. A *subunit* can be a single protein or a group of few proteins. Shells made of identical subunits will be regular in shape

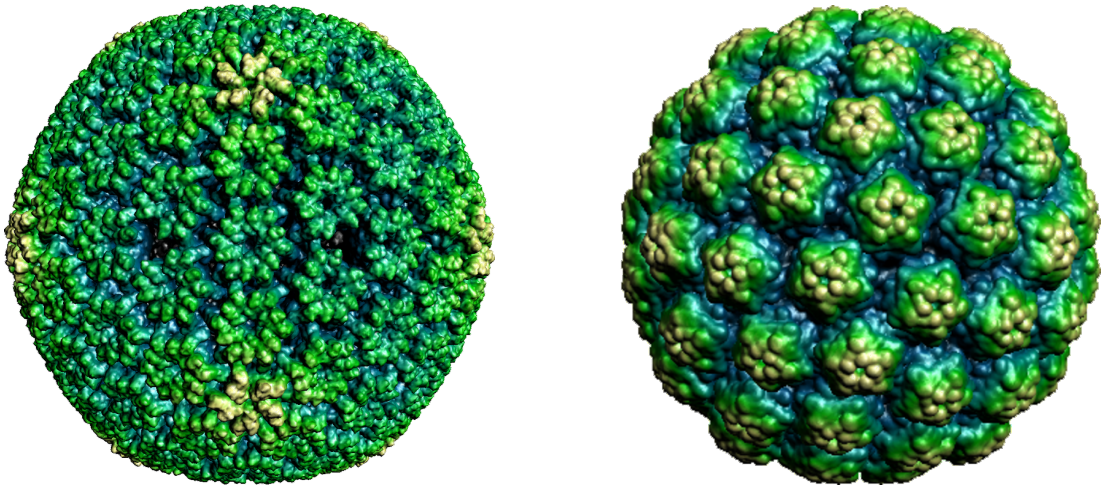

(a) Cytomegalovirus. (b) Polyomavirus.

Figure 1.1: Quasispherical viruses can be of polyhedral shape like a Cytomegalovirus [YJJ17] or of spherical shape like a Polyomavirus [SEN11].

and uniform in size. The environment of a subunit is characterized by the number of neighbors, the number of bonds, bonding sites etc. Their theory suggests that since the subunits are identical, they should be indistinguishable in terms of their environment. This is called the theory of *strict equivalence*. Since all the subunits are in identical environments the overall structure should be isometric. Only cubic point-groups *viz.* tetrahedral, octahedral and icosahedral can give rise to isometric structures because all the three coordinate directions for these groups are equivalent. Although the subunits themselves may be asymmetric, they can be arranged into *units* which are symmetric. A *unit* of three asymmetric subunits can be arranged on triangular faces of a tetrahedron, octahedron or an icosahedron such that each unit is symmetric to the units on all other faces of the structure. This suggests that tetrahedral, octahedral and icosahedral structures should be made up of 12, 24 and 60 subunits respectively. Such a structure would satisfy the requirement of strict equivalence. Of the three cubic point-groups, icosahedral structure is the closest to a sphere and hence provides the maximum volume to surface-area ratio. Thus, one can get maximum enclosed volume for a fixed number of subunits in an icosahedral structure. Therefore, icosahedral structures are preferable for forming viral shells over tetrahedral or octahedral structures. Figure 1.2

shows an icosahedral structure which satisfies strict equivalence. Several electron microscope

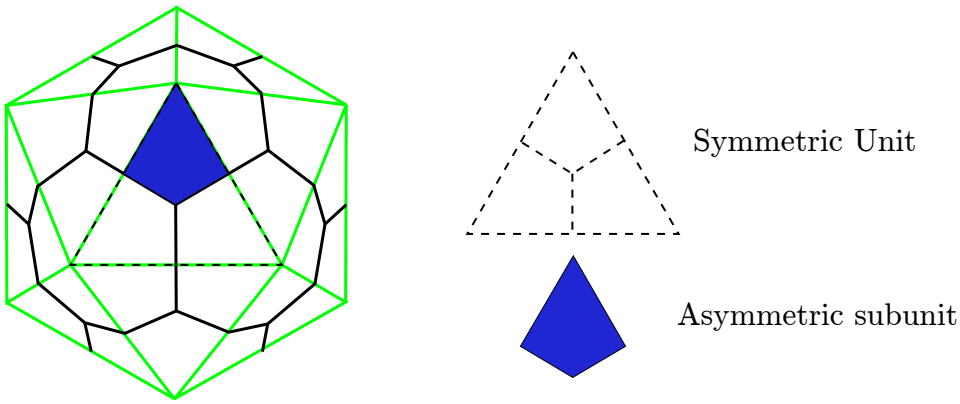

Figure 1.2: A symmetric unit composed of asymmetric subunits can be arranged into an icosahedral structure that obeys strict equivalence. The figure was adapted from VIPERdb (http://viperdb.scripps.edu) [CSB09]

experiments like [WS58] and X-ray diffraction investigations like [FK59] of unrelated viruses showed that icosahedral symmetry was indeed predominant in viral shells. But the number of subunits was not found to be 60 or even a multiple of 60. To explain this discrepancy, Caspar and Klug [CK62] proposed their theory of *quasi-equivalence*. They relaxed the requirement that each subunit should have exactly equivalent environment. They analyzed the problem of forming closed shells from triangular units as a topological problem of tiling a triangular or a hexagonal lattice on the surface of a sphere. Such a closed shell would form a polyhedral surface. As per Descartes-Euler polyhedral formula [Wei], the Euler-Poincaré characteristic χ for a polyhedral surface is given as

$$\chi = V - E + F = 2 \tag{1.1}$$

where V is the number of vertices, E is the number of edges and F is the number of faces. It can be shown that equation 1.1 cannot be satisfied if each vertex of the closed shell has exactly 6 neighbors like a flat triangular lattice. We must allow some vertices to have more or fewer neighbors. It can also be shown that if we allow some vertices to have 5 neighbors there should be exactly 12 such vertices to satisfy equation 1.1. This is called "geometric frustration". Since the triangles forming the polyhedron correspond to a group of subunits

of a viral shell, the subunits on triangles associated with a five-fold vertex will have slightly different environment than the subunits lying on triangles with a six-fold vertex. Thus, this supports the theory of quasi-equivalence. Subunits associated with five-fold vertices are called *pentamers* whereas those associated with six-fold vertices are called *hexamers*. By extension, we can also define *heptamers*.

The arguments presented in the previous paragraph can be used to systematically characterize icosahedral structures of different sizes. Consider a triangular lattice as shown in

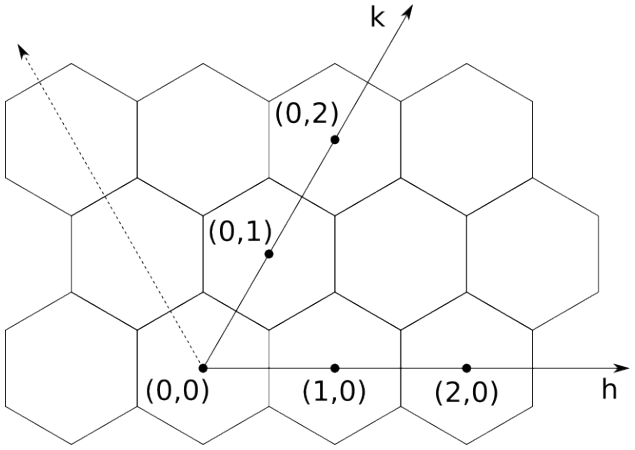

Figure 1.3: We can setup a coordinate system setup in a hexagonal lattice using two axes separated by 60°. A unit length along either axis measures the distance between neighboring hexagons. The choice of the axes is not unique.

Figure 1.3. In order to fold this lattice into a closed shell, we need to create exactly 12 five-fold vertices in this lattice, as discussed before. We can do this by cutting out triangles from some of the hexagons and joining the newly formed edges to create pentagonal pyramids as shown in Figure 1.4. To form icosahedral structures, we need to distribute the 12 five-fold vertices over the lattice in a systematic pattern. Rather, it can be shown that the distance between any two five-fold vertices as measure along the h and k axes of Figure 1.3 should be constant. Farther the five-fold sites are situated from one another, bigger will be the size of the resultant icosahedron. The distance can be expressed as T number where

$$T = h^2 + k^2 + hk \tag{1.2}$$

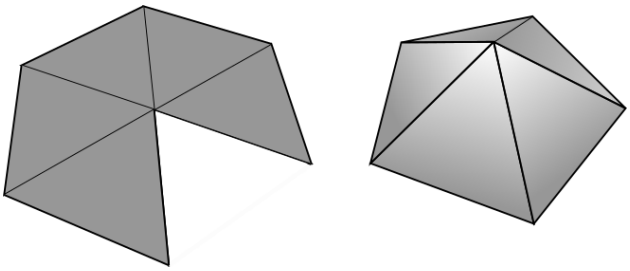

Figure 1.4: We can cut-out a triangle from a hexagon and join the new edges to form a pentagonal pyramid with equilateral triangular faces. If we try to join the edges while keeping the structure flat instead of forming a pyramid, the faces will no longer remain equilateral and the edges will be under a lot of strain.

Figure 1.5 shows a *template* obtained by cutting out appropriate triangles from a hexagonal lattice such that when we join the edges associated with the cut-out triangles we will get an icosahedron with 20 faces. The folded structure is same as the one shown in Figure 1.2. In this case, the distance between any two five-fold sites can be expressed as $(h = 1, k = 0)$ or $(h = 0, k = 1)$, both of which give $T = 1$ based on Equation 1.2. So, this structure is called a $T = 1$ structure and it is the smallest icosahedron that we can make. Equation 1.2 also

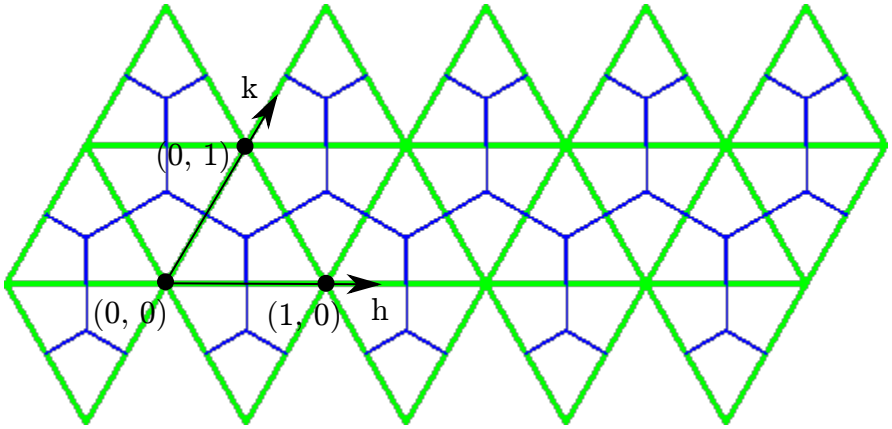

Figure 1.5: The flat hexagonal lattice template with appropriate triangles cut-out so that by joining the edges of the cut-out triangles we get an icosahedron with $T = (1, 0)$ or $T = (0, 1)$. This figure was adapted from VIPERdb (http://viperdb.scripps.edu) [CSB09].

contains information about chirality of the resultant icosahedron. If $h \neq k$ and neither of them is zero, the structure is chiral. On the other hand, if $h = k$ or if one of them is zero,

the structure is achiral. A chiral structure is right-handed when $h > k$ and it is left-handed when $h < k$. The T number of a shell also gives us information about the number of

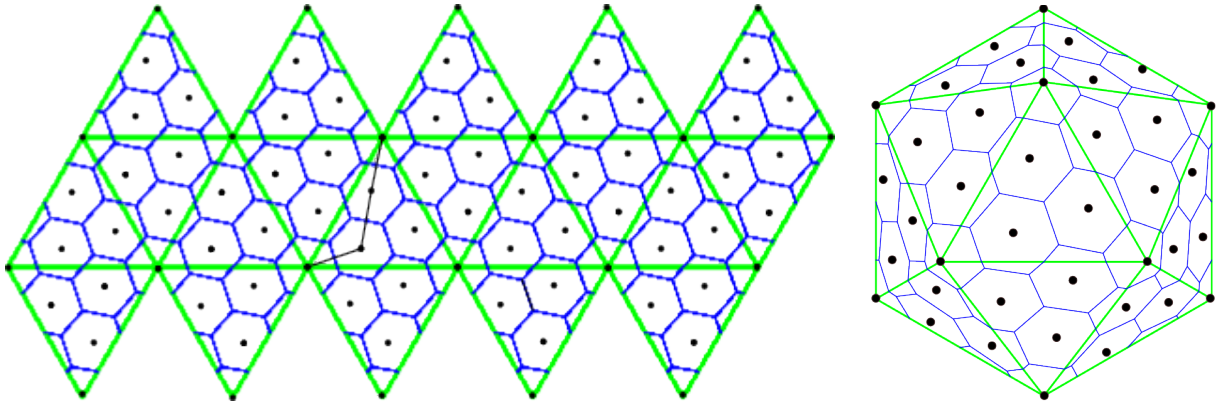

(a) Template for ($h = 1$, $k = 2$) shell. (b) Left-handed $T = 7$ shell.

Figure 1.6: The $h = 1$, $k = 2$ configuration of $T = 7$ Caspar-Klug shell has been shown. It is a left-handed chiral structure whose mirror image is shown in Figure 1.7.

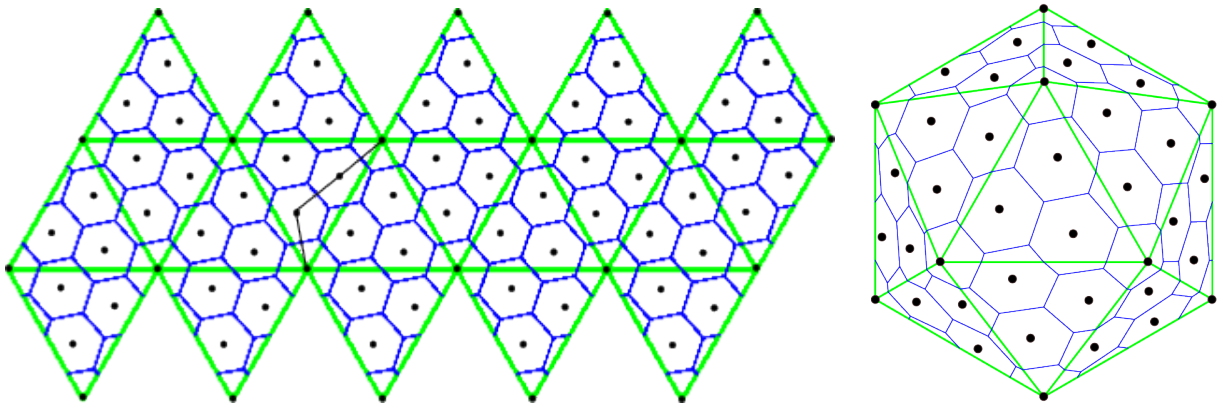

(a) Template for ($h = 2$, $k = 1$) shell. (b) Right-handed $T = 7$ shell.

Figure 1.7: The $h = 2$, $k = 1$ configuration of $T = 7$ Caspar-Klug shell has been shown. It is a right-handed chiral structure whose mirror image is shown in Figure 1.6.

vertices, N, that constitute the shell

$$N = 10T + 2. \tag{1.3}$$

The first ten T numbers and the corresponding number of particles/vertices in the shells have been listed in Table 1.1. It is clear from the table that to form icosahedral shells we

need a specific number of particles. We cannot take any arbitrary number of particles and arrange them into a perfectly icosahedral shell. Experimental observations have confirmed that the number of particles predicted by the Caspar-Klug construction indeed match up with the number of subunits observed in various icosahedral viral shells.

h	k	T	N	Chiral?
1	0	1	12	No
1	1	3	32	No
2	0	4	42	No
2	1	7	72	Yes
2	2	12	122	No
3	0	9	92	No
3	1	13	132	Yes
3	2	19	192	Yes
3	3	27	272	No
4	0	16	162	No

Table 1.1: The 10 smallest values of h and k coordinates of Caspar-Klug construction have been tabulated. These give the 10 smallest T numbers and the corresponding number of vertices that form the shells.

Now that we have a systematic way to describe structures of viral shells we can proceed with studying their mechanical behavior.

1.2 Continuum Theory of Shells

It is found that the structure into which a virus self-assembles in vitro depends on environmental conditions like salt concentration and pH values [AB76, BBW69, LGP09, GLK99, HBW08]. This implies that their structures are a result of free energy minimization of the interactions between their subunits [ZRB04, LZR10, Zlo03]. We can, therefore, write

Hamiltonians for which the structures discussed in Section 1.1 are the minimum energy configuration.

Intuitively, we can understand that if we try to cut out triangles from a hexagonal lattice and join the newly formed edges, as discussed in Section 1.1, while constraining the lattice to remain flat we would induce a large strain in the lattice. The farther we travel radially away from the five-fold site the strain goes on increasing more and more. But if allow the lattice to bend out of plane then it can release a lot of the strain around the five-fold sites. In a hexagonal lattice, a dislocation refers to a pair of a pentamer and a heptamer situated side by side whereas a disclination indicates an isolated pentamer or a heptamer in a regular hexagonal lattice. Seung and Nelson [SN88] studied the elasticity theory of flexible membranes (i.e. membranes that can bend out of plane) in presence of dislocations and disclinations. They found that a transition from a flat to a *buckled* structure occurs when

$$\gamma = \frac{YR^2}{\kappa} \geq 154 \tag{1.4}$$

where Y is the 2D Young's modulus of the membrane, R is disk radius and κ is the bending modulus. γ is a dimensionless number, called the Föppl von Kármán (FvK) number, that measures comparative resistance of the membrane to in-plane stretching versus out-of-plane bending deformation. For higher values of γ, the membrane prefers to minimize the in-plane strains induced by the presence of a five-fold site at the cost of bending out of plane, as indicated in Figure 1.4. The presence of disclinations introduces stress in the lattice.

Lidmar *et al* [LMN03] investigated the question whether closed shells also exhibit buckling behavior as found by Seung and Nelson [SN88]. While the answer seems to be obviously a 'yes', we need to consider the increased complexity of the problem due to interactions between deformations around neighboring five-fold sites. The energy used in this analysis is given as

$$\begin{aligned}\mathcal{H} &= \mathcal{H}_{\text{stretching}} + \mathcal{H}_{\text{bending}} \\ &= \frac{1}{2}\int_S \mathrm{d}S\left(2\mu u_{ij}u_{ij} + \lambda u_{kk}^2\right) + \frac{1}{2}\int_S \mathrm{d}S\left(4\kappa H^2 + 2\kappa_G K\right).\end{aligned} \tag{1.5}$$

where μ and λ are the Lamé coefficients, κ_G is the Gaussian modulus, κ is the bending modulus, H is the mean curvature and K is the Gaussian curvature of the membrane. The bending energy term is called as the Helfrich bending energy and it is widely used for modeling lipid bilayer membranes. u_{ij} is the strain tensor given by

$$u_{ij} = \frac{1}{2}\left(u_{i,j} + u_{j,i} + f_{,i}f_{,j}\right) \tag{1.6}$$

where u_1 and u_2 are in-plane deformations and f is out-of-plane deformation such that a point that was at $(x_1, x_2, 0)$ in the reference state goes to $(x_1 + u_1, x_2 + u_2, f)$. Thus, the reference state is a flat hexagonal lattice which can be folded into an icosahedral shell without incurring any strain as discussed in Section 1.1. So, we can also say that the icosahedral shell is the stress free configuration. For closed shells, by Gauss-Bonnet theorem,

$$\oint_S \mathrm{d}S\, K = 4\pi. \tag{1.7}$$

Therefore, the Gaussian curvature term in Equation 1.8 reduces to a constant and can be ignored from our calculations for energy minimization. The effective total energy is reduced to

$$\mathcal{H} = \frac{1}{2}\int_S \mathrm{d}S\,(2\mu u_{ij}u_{ij} + \lambda u_{kk}^2) + 2\int_S \mathrm{d}S\,\kappa H^2. \tag{1.8}$$

The 2D Young's modulus and the Poisson's ratio can be expressed in terms of the Lamé coefficients as

$$Y = \frac{4\mu(\mu+\lambda)}{2\mu+\lambda} \quad \nu = \frac{\lambda}{2\mu+\lambda}$$

Rearranging gives

$$\mu = \frac{Y}{2(1+\nu)} \quad \lambda = \frac{Y\nu}{1-\nu^2}$$

We can rewrite Equation 1.8 as

$$\mathcal{H} = \frac{1}{2}\int_S \mathrm{d}S\left(\frac{Y}{1+\nu}u_{ij}u_{ij} + \frac{Y\nu}{1-\nu^2}u_{kk}^2\right) + 2\int_S \mathrm{d}S\,\kappa H^2. \tag{1.9}$$

For numerical analysis, the lattice vertices can be treated as being connected with harmonic springs with spring constant ϵ. If we let the mean lattice spacing be a, then Equation 1.9

can be discretized [LMN03] as

$$\mathcal{H} = \frac{\epsilon}{2} \sum_{\langle ij \rangle} \left(|\mathbf{r}_i - \mathbf{r}_j| - a \right)^2 + \frac{\tilde{\kappa}}{2} \sum_{\langle IJ \rangle} \left(\hat{\mathbf{n}}_I - \hat{\mathbf{n}}_J \right)^2 \tag{1.10}$$

where $\langle ij \rangle$ denote bonds between nearest neighbors and $\langle IJ \rangle$ represent a pair of unit normals associated with neighboring triangles in the lattice. Also, the spring constant ϵ, the Poisson's ratio and the discrete bending modulus $\tilde{\kappa}$ are given as

$$\epsilon = \frac{\sqrt{3}}{2} Y \quad \nu = \frac{1}{3} \quad \tilde{\kappa} = \frac{2}{\sqrt{3}} \kappa \tag{1.11}$$

It is found that the minimum energy structures depend only on the FvK number.

Lidmar *et al* introduce a quantitative measure of deviation of a closed shell from a perfect sphere, called as the *asphericity*, given by

$$\alpha = \frac{\langle \Delta R^2 \rangle}{\langle R \rangle^2} = \frac{1}{N} \sum_{i=1}^{N} \frac{\left(R_i - \langle R \rangle \right)^2}{\langle R \rangle^2} \tag{1.12}$$

where the mean radius is

$$\langle R \rangle = \frac{1}{N} \sum_{i=1}^{N} R_i$$

They find that the asphericity of the minimum energy shell changes as a function of the FvK number as shown in Figure 1.8. There is a sharp but continuous decrease in asphericity around $\gamma = 200$. This is called as the *buckling transition*. At low values of γ the shell is spherical whereas at high values of γ it is faceted like a polyhedron. FvK number is directly proportional to R^2 as noted in Equation 1.4. Thus, the continuum theory of shells predicts that viruses with larger shells should be faceted whereas viruses with smaller shells should be spherical. Indeed, this is in agreement with experimental observations. For example, the radius of Cytomegalovirus and Polyomavirus shown in Figure 1.1 are 200 nm and 50 nm and they have polyhedral and spherical shapes respectively.

1.3 Beyond the Continuum Theory

There are more elaborate versions [Agg18, KRW12] of continuum theory shell models that consider stress-free reference configuration other than the icosahedral state as done in Sec-

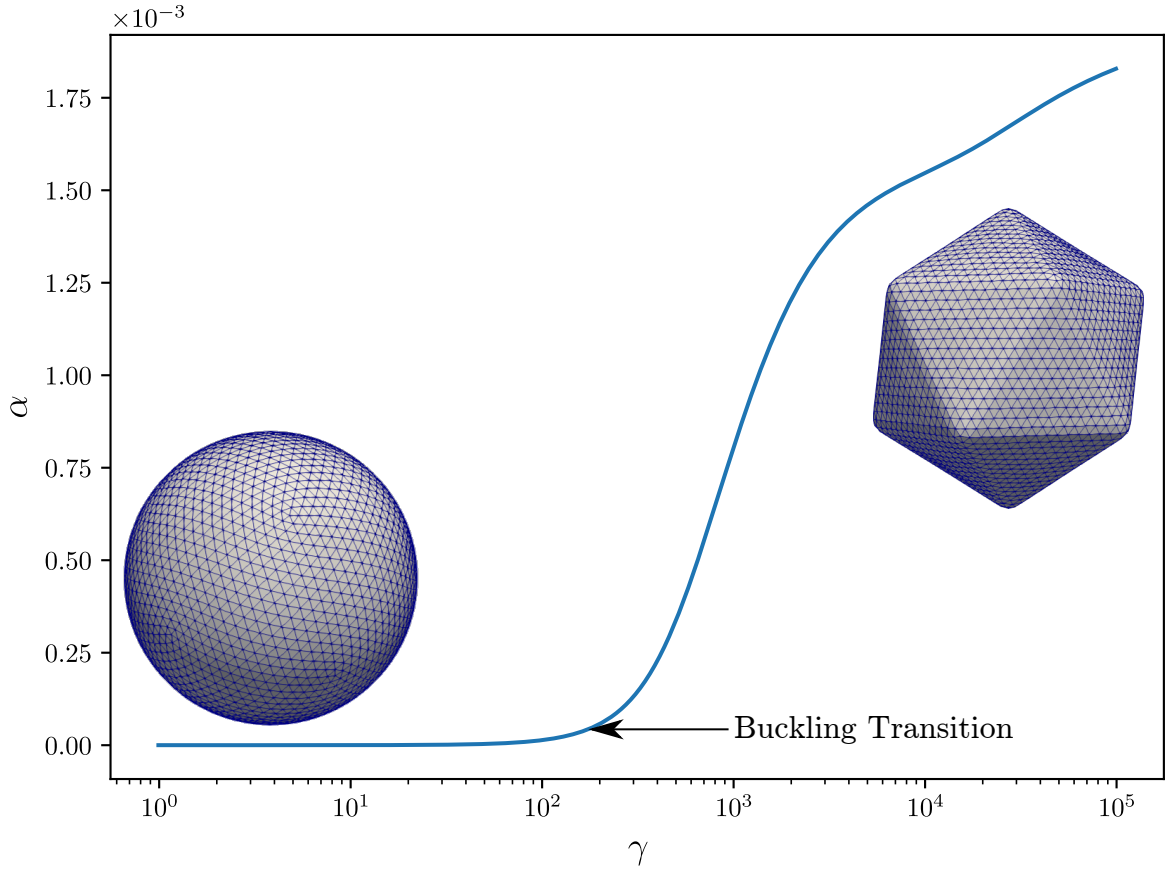

Figure 1.8: The asphericity α of a Caspar-Klug shell varies as a function of the FvK number γ of the shell. The sharp decrease in the asphericity at $\gamma = 200$ is called as the *buckling transition*. At low FvK numbers, the shell is spherical whereas at high FvK numbers it becomes faceted like a polyhedron.

tion 1.2. These theories have been successfully used to explain important results like structural failure of viral shells [KBM06] and determination of pre-stress [KRW12, Agg18] in these shells. The continuum description is certainly a very useful tool for studying viruses. It is even surprising that the continuum description works so well for these structures which are on the nanoscale. It is natural to expect that considering the molecular details of the constituent proteins of the shells is important at this scale. This would warrant the use of all-atom simulations using techniques of molecular dynamics. Such an approach is valuable because it can provide results for shells of specific viruses made up of specific set of proteins

though at the expense of computational time and effort. Thus, we have two extremes — a continuum description and an atomistic description. Taking a balanced approach between these two extremes, our interest for the next two chapters is to study the *general effects of discreteness* of the viral shells without considering any microscopic details. Thus, our aim is to develop *coarse grained* models where we will treat protein units (also called as *capsomers* which may be a pentamer, a hexamer etc.) as point particles interacting via suitable potentials. We will accomplish this in two steps. In Chapter 2, we will replace only the in-plane stretching energy of the shell with sum of discrete potential interactions while retaining the continuum Helfrich model for the bending energy. In Chapter 3 we will replace even the bending energy with discrete potentials.

Our motivation for studying discrete shells is as follows. In the continuum model, the minimum energy configuration of the shell always has an icosahedral symmetry in the absence of any external applied loads. This seems to suggest that the icosahedral structure is stable at all FvK numbers. But we must take into account that the icosahedral structure is also the assumed stress-free reference state of the continuum model. Besides, because of the assumption of isotropy, as there are only two independent constitutive parameters, the continuum model always gives a structure with icosahedral symmetry as the minimum energy configuration. So, the stability of icosahedral symmetry may be a little misleading. In fact, it is well known from a study of close-packing of disks on a sphere (Tammes problem) and other similar studies [ZRB04] that the icosahedral symmetry is not always stable. For example, when the number of disks exceeds 72, there are other competing symmetries as reported in [ZRB04]. Further, we are interested in investigating thermal response of shells like melting. Melting implies that the particles forming the shell can freely move past each other like in a fluid. As long as we model the particles as nodes of a finite element mesh surface, there will be many challenges to modeling such flow like the need to remesh at every time step. Therefore, to model such behavior, discrete models are certainly better suited.

CHAPTER 2

Hybrid Shell Model

In this chapter we will set-up a hybrid discrete-continuum model of shells. The key idea is to replace the harmonic springs of Equation 1.10 with Morse potential which we will discuss in detail in Section 2.1. The main result is that upon proper choice of Morse potential parameters the buckling transition coincides with a mathematical singularity which we will see in Section 2.4. We will explain this behavior by analyzing a toy model of a pentagonal pyramid in Section 2.3.

2.1 Model

Physically, the hybrid model represents a collection of interacting particles lying on the surface of a closed shell. The surface resists bending but offers no resistance to in-plane stretching. The in-plane stretching resistance is entirely due to the interactions between the particles. The energy equation for this discrete-continuum model is

$$\mathcal{H} = \sum_{\langle ij \rangle} V(r_{ij}) + 2 \int_S \kappa H^2 \, \mathrm{d}S \tag{2.1}$$

where $\langle ij \rangle$ represents a bond between a pair of nearest neighbors and $V(r)$ is a suitable potential. κ is bending modulus of the surface and H is the mean curvature of the surface. The bending energy depends only on the curvature of the surface and is independent of the parametrization. Physically, this means that it represents a fluid surface where the particles can move freely in the surface. This surface cannot sustain any stretching or shearing. It can only resist normal forces and deformation.

There are different choices for $V(r)$ available. Harmonic potential does not allow particles

to escape the influence of their neighbors. Rather, farther the particles move from each other stronger the pull they experience towards each other. We need a potential that has long range attraction but only up to a cut-off distance beyond which the potential decays to zero quickly. Both Lennard-Jones potential and Morse potential satisfy this requirement. Lennard-Jones potential is defined as

$$V_{\mathrm{LJ}}(r) = V_e\left[\left(\frac{r_e}{r}\right)^{12} - 2\left(\frac{r_e}{r}\right)^{6}\right] \tag{2.2}$$

where r_e is the equilibrium separation and V_e is the equilibrium potential. These are the two control parameters for this potential. Lennard-Jones potential is a common choice for modeling viral shells [FCW10, WOB12, BDT16, ZR05]. But we will use Morse potential because it also allows us to control the width of the potential well independently of r_e and V_e. The Morse potential is defined as

$$V(r) = V_M\left[e^{-2a(r-r_e)} - 2e^{-a(r-r_e)}\right] \tag{2.3}$$

where r_e is the equilibrium separation and V_M is the equilibrium potential. The parameter a has dimensions of $[L]^{-1}$ and it controls the width of the potential well. We can define a non-dimensional width of the Morse potential well as

$$\delta = \frac{\ln 2}{a\, r_e} \tag{2.4}$$

Figure 2.1 shows the variation of Morse potential with distance and the meaning of the three parameters that control it. For distances shorter than r_e there is a strong repulsion and for distances larger than r_e there is attraction. At distance $r_e + \delta r_e$ there is an inflection point beyond which the potential decays to zero. When particles are separated by a distance equal to that of the inflection point, the strain in the bond is equal to δ. So δ has the physical significance of being the *fracture strain*. In order to define a FvK number for the hybrid model, we need an expression for the 2D Young's modulus Y. We can substitute the spring constant $\epsilon = V''(r_e)$ in Equation 1.11 to write

$$Y = \frac{2}{\sqrt{3}}V''(r_e) = \frac{4}{\sqrt{3}}V_M a^2 \tag{2.5}$$

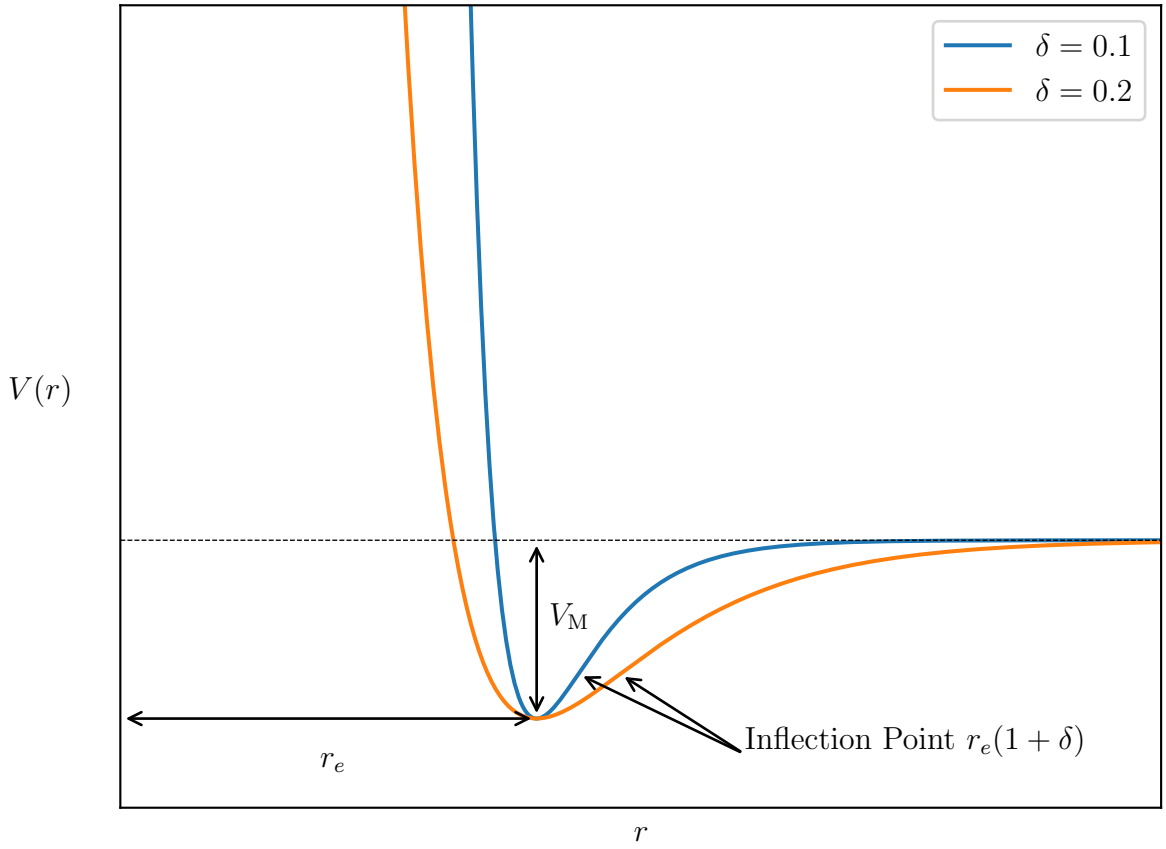

Figure 2.1: Morse potential parameters have been shown. The dotted lines marks zero potential. r_e is the equilibrium separation and V_M is the potential at equilibrium separation. δ controls the position of inflection point which is located at $r_e(1+\delta)$.

2.2 Discretized Bending Energy

For numerical simulations we need to discretize the bending energy. We start by creating a mesh by connecting every particle with its nearest neighbors which are identified using the Voronoi criterion [Vor08]. We used finite element method to discretize the bending energy following the methodology presented in [FK06]. This work uses C^1 conforming Loop subdivision shell finite elements [COS00] with positions of the particles as the vertices of the mesh. It is important to note that the shape functions associated with the Loop shell subdivision finite elements are non-interpolating. This means that the surface defined by the particles of the closed shell does not pass through the particle positions. This has been shown

in Figure 2.2. The surface is just a way to capture the bending interactions of capsomers that form the shell of a virus. It does not represent an actual membrane of the shell. Hence, the fact that the surface does not interpolate the particle positions is not a flaw in this model. Fluidity of the Helfrich bending energy, as noted in Section 2.1, creates problems for the finite-element solver because of the zero-energy stretching and shearing modes. But in our problem, the nodes of the surface mesh also represent interacting particles which resist stretching and compression. Thus, we are able to circumvent the degeneracy issue.

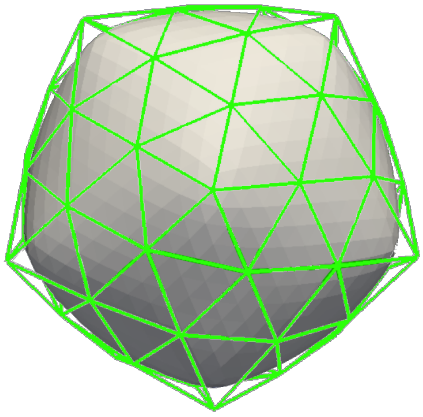

Figure 2.2: The discretized setup for the hybrid model has a surface defined by Loop shell subdivision finite elements shape functions indicated as the grey surface. The green lines represent the bonds between nearest neighbors. All the vertices of the mesh represent capsomers of virus shell. As can be seen here, the surface does not interpolate the vertices of the mesh.

The pentamers represent a disclination in a flat hexagonal lattice [SN88]. Hence, they are centers of stress concentration even for the closed shell. We expect the stresses in the bonds associated with the pentamers to play a key role in determining the minimum energy configuration. Therefore, in the next section we will analyze the forces associated with edges of a pentagonal pyramid formed by the six particles of the pentamer.

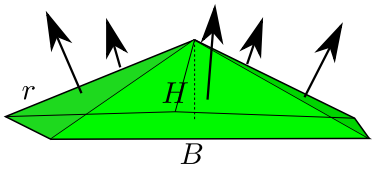

Figure 2.3: A pentagonal pyramid with vertices representing interacting particles. The base edge length is B and the length of edges joining the apex to base vertices is r. H denotes height of the pyramid and the black arrows are the unit surface normals of the triangular faces.

2.3 Analysis of Bond Forces of a Pentamer

Figure 2.3 shows a pentamer consisting of six particles — one at the apex and five at the base of a pentagonal pyramid of height H. Let B be the edge length of the base pentagon and r be the length of the edges joining the apex to the vertices of the base. The outward surface normals of the triangular faces will be used to estimate the bending energy of the structure. The energy of this structure can be approximated using an equation similar to Equation 1.10.

$$\mathcal{H} \simeq \sum_{\langle ij \rangle} V(r_{ij}) + \frac{\tilde{\kappa}}{2} \sum_{\langle IJ \rangle} (\hat{n}_I - \hat{n}_J)^2 \tag{2.6}$$

where $\tilde{\kappa} = \frac{2}{\sqrt{3}}\kappa$ [SN88].

First assume $\kappa = 0$. In that limit, the triangles are equilateral in the minimum energy state while B and r are equal to the equilibrium spacing r_e. For non-zero κ, the orientational energy effectively generates a compression force on the apex of the pyramid of the order of κ/r_e. This force stretches the bonds along the base and compresses the bonds linking the apex particle to the base. As κ increases, the pyramid is progressively flattened (see Figure 2.4).

It follows that in the fully flattened state $r = B/(2\sin 36^\circ)$. The condition that the net force on the five base particles is zero in the flattened state is:

$$2V'(B)\cos 54^\circ = -V'(B/(2\sin 36^\circ)). \tag{2.7}$$

The solution of this equation determines the base edge-length B. For the flattened state

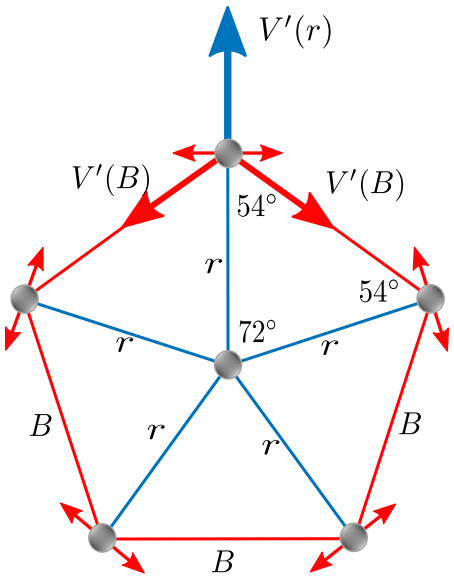

Figure 2.4: The force diagram for vertices of a flattened pentagonal pyramid have been shown. Blue color represents compression and red color indicates elongation. B is the length of a side of the basal pentagon. r is the length of an edge connecting the apex to the basal vertices. The double headed arrows indicate the lowest energy mode of displacement of the vertices in the azimuthal direction.

to be stable, the energy cost for in-plane displacements must be positive. There are nine in-plane modes excluding rigid-body rotation. For the lowest energy modes, particles are displaced in the direction perpendicular to the line joining the base particles and the apex. Number the five base particles by $j = 1$ to 5. If θ_j is the angular displacement of particle j, then the displacement energy, δE, in the limit of small θ equals

$$\delta E = \frac{1}{2} V''(B)(r \sin 36^\circ)^2 \sum_{j=1}^{5} (\theta_{j+1} - \theta_j)^2, \tag{2.8}$$

where $\theta_6 = \theta_1$. The four mode energies have the sign of $V''(B)$ so if B exceeds the inflection point $r_e + (1/a) \ln 2$, then the flattened pyramid state is mechanically unstable because δE in Equation 2.8 changes sign. At the point of instability, one of the five bonds linking the base particles fractures while the remaining bond lengths relax to their equilibrium spacing. The five triangles once again become equilateral. To determine the value of B at the point

of instability, let us first write $V'(x)$ for the Morse potential as

$$V'(x) = 2aV_M \left(e^{-a(x-r_e)} - e^{-2a(x-r_e)}\right) \tag{2.9}$$

Substituting $x = B = r_e(1+\delta)$ in Equation 2.9 and then substituting Equation 2.9 in Equation 2.7 gives

$$4aV_M \cos\left(\frac{3\pi}{10}\right)\left[e^{-a(B-r_e)} - e^{-2a(B-r_e)}\right] = -2aV_M\left\{e^{-a\left[\frac{B}{2\sin(\pi/5)}-r_e\right]} - e^{-2a\left[\frac{B}{2\sin(\pi/5)}-r_e\right]}\right\} \tag{2.10}$$

Let's substitute $2\cos(3\pi/10) = 2\sin(\pi/5) = C$ and $a = \ln 2/\delta r_e$ (from Equation 2.4) in Equation 2.10. On simplifying, we get

$$\frac{C}{4} = 2^{\frac{C-\delta-1}{C\delta}}\left(2^{\frac{C-\delta-1}{C\delta}} - 1\right) \tag{2.11}$$

Equation 2.11 has two solutions

$$\delta_1 = \frac{\ln\left(2^{\frac{C-1}{C}}\right)}{\ln\left(2^{\frac{-C+1}{C}}\left(\sqrt{C+1}+1\right)\right)} \approx 0.12896 \tag{2.12}$$

and

$$\delta_2 = \frac{(C-1)\log(2)}{C\log\left(-\sqrt{C+1}+1\right) - (C-1)\log(2)} \approx -0.00829 - 0.0307i \tag{2.13}$$

Keeping only the real solution, we get $B/r_e \simeq 1.13$ and $r \simeq 0.96r_e$. Therefore, for values of $\delta < 0.13$, the flattened pentagonal state becomes unstable to in-plane displacements resulting in a fractured state as shown in Figure 2.5.

Now let us consider the stability of the flattened state to out-of-plane displacements of the apex. By dimensional argument, the effect of bending energy term in Equation 2.6 is to apply a compressive force of the order κ/r_e on the edge joining the apex and the base particles. This is opposed by an elongating force $V'(r)$ due to repulsion between the base and the apex particles. The flattened state is stable when the compressive force exceeds the elongating force i.e. $\kappa > r_e V'(r)$. Using $r \simeq 0.96r_e$ we can approximate

$$|V'(r)| \simeq |V'(r_e - 0.04r_e)| = |\cancel{V'(r_e)} - 0.04r_e V''(r_e)| = 0.04r_e V''(r_e) \tag{2.14}$$

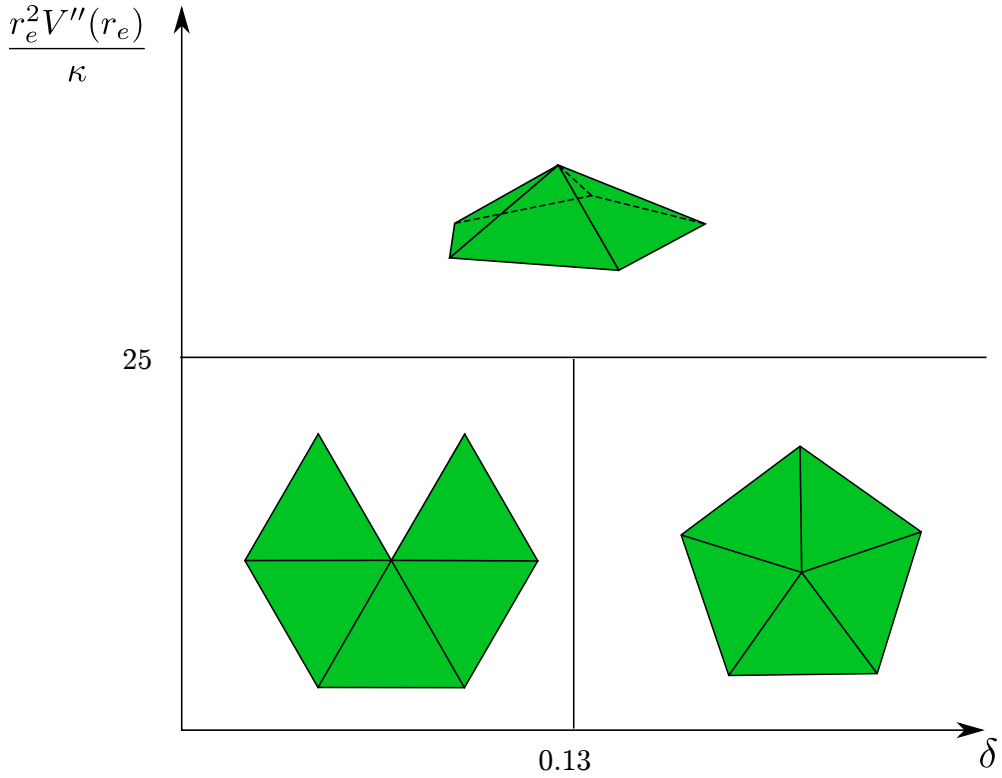

Figure 2.5: Stability diagram of a pentagonal pyramid as a function of dimensionless width of the Morse potential δ and an effective FvK number $\gamma_{\text{eff}} = \frac{r_e^2 V''(r_e)}{\kappa}$. For values of $\gamma_{\text{eff}} > 25$ the pyramid structure is stable whereas for lower values a flattened state is stable. In the flattened state, there is a fracture for values of $\delta < 0.13$.

Therefore, we can say that for the flattened state is stable against out-of-plane displacements for

$$\frac{r_e^2 V''(r_e)}{\kappa} > 25 \tag{2.15}$$

The full stability diagram for in-plane and out-of-plane displacements has been shown in Figure 2.5.

In the next section, we will present results obtained by numerical energy minimization of Equation 2.1 for increasing numbers of particles that form Caspar-Klug structures.

2.4 Results of Numerical Energy Minimization

In the previous section, we found that the pentagonal flat state develops a fracture when the dimensionless width δ of the Morse potential falls below a critical value. We validated this numerically for a $T = 7$ structure. We calculated the asphericity versus FvK number plots for various values of δ. It is found that for $\delta < 0.10$, a mathematical singularity appears near the buckling transition. Figure 2.6 shows the asphericity curves for $\delta = 0.11, 0.10$ and 0.09. If δ is increased from 0.09 to 0.1 then the stability range of the state with icosahedral

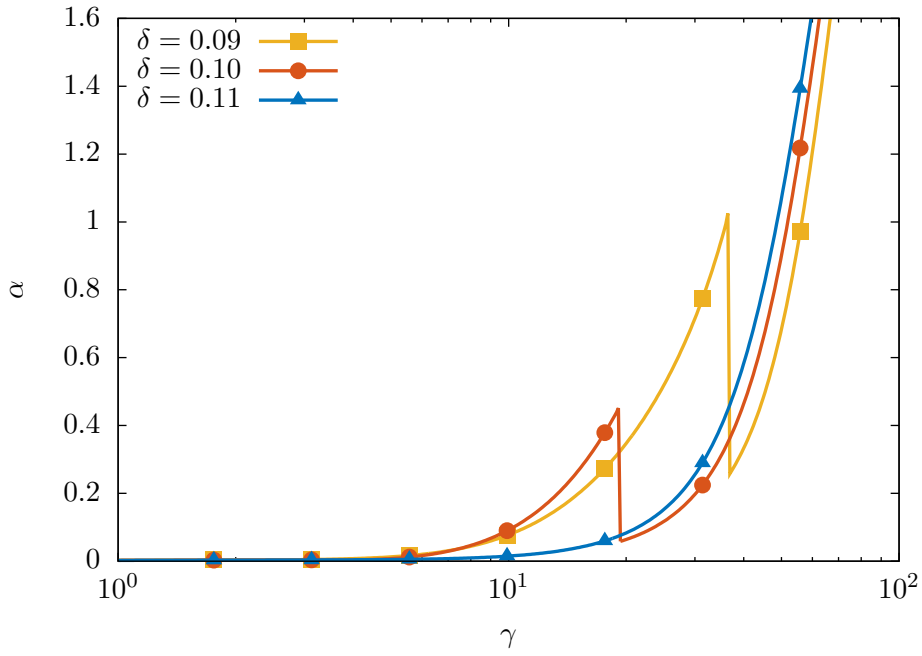

Figure 2.6: Asphericity α as a function of FvK number γ for $N = 72$ particles for varying widths of the Morse potential well δ near the buckling transition. There is no instability for $\delta = 0.11$ but $\delta = 0.10$ marks the onset of instability which becomes aggravated for $\delta = 0.09$.

symmetry is increased while the magnitude of the asphericity jump is reduced. For $\delta = 0.11$ icosahedral symmetry is stable over the whole range of FvK Numbers. Thus, structural instability is indeed restricted to smaller values of δ. The critical value for dimensionless well-width, δ_c, (e.g., 0.10 for $N = 72$) found in our numerical simulations is below the value of 0.13 obtained for the toy model of Section 2.3 for isolated pyramids. In addition, the critical value for γ depends on δ. One reason for the discrepancy is that, even though no

external forces are exerted on the pyramids just before the onset of instability, the unstressed bonds linking the pyramids increase the restoring force for the in-plane deformation mode. As a result, the instabilities of the different pyramids are in fact coupled.

In Section 2.1 we discussed that the dimensionless width of the Morse potential δ can be interpreted as a fracture strain. If δ is increasingly reduced, the Morse bonds between neighboring particles fracture at progressively smaller strains, i.e., the particles escape the influence of their neighbors' Morse potential at values of r closer to r_e. Thus, for a value of δ much lower than the critical value δ_c the shell becomes *brittle* and instead of a single instability we encounter a complex sequence of discontinuities in the asphericity versus FvK number plot.

To obtain the ground state energy of the shells, we minimize the energy of Equation. 2.1 using the Limited Memory-BFGS algorithm [ZBL97]. This is a steepest-gradient minimization method with line search to solve for particle positions at every FvK number. The triangular network and the associated C^1 surface are updated as particles move to new positions. The dimensionless potential width, δ, and the dimensionless FvK number, γ, — estimated from the Young's Modulus of the flat hexagonal lattice — are the only two free parameters. In our calculations, energies and forces have been non-dimensionalized with respect to the parameters of Morse potential — energies have been non-dimensionalized with respect to V_M, and forces have been non-dimensionalized with respect to V_M/r_e. For a given N, we always started from isometric Caspar-Klug shells with an FvK number of 10^5. We then reduced the FvK number to 1 in 2000 log-scaled steps. Finally, γ was increased back to its initial value using the same steps.

2.4.1 $N = 72$

The first shell was constructed from $N = 72$ particles. The isometric starting structure was one of the two isomers of the chiral $T = 7$ icosahedral shell (Figure. 1.6) with 72 particles located at the centers of 12 pentamers and 60 hexamers. Figure. 2.7 shows the dependence of the asphericity α on the FvK Number γ for $\delta = 0.09$.

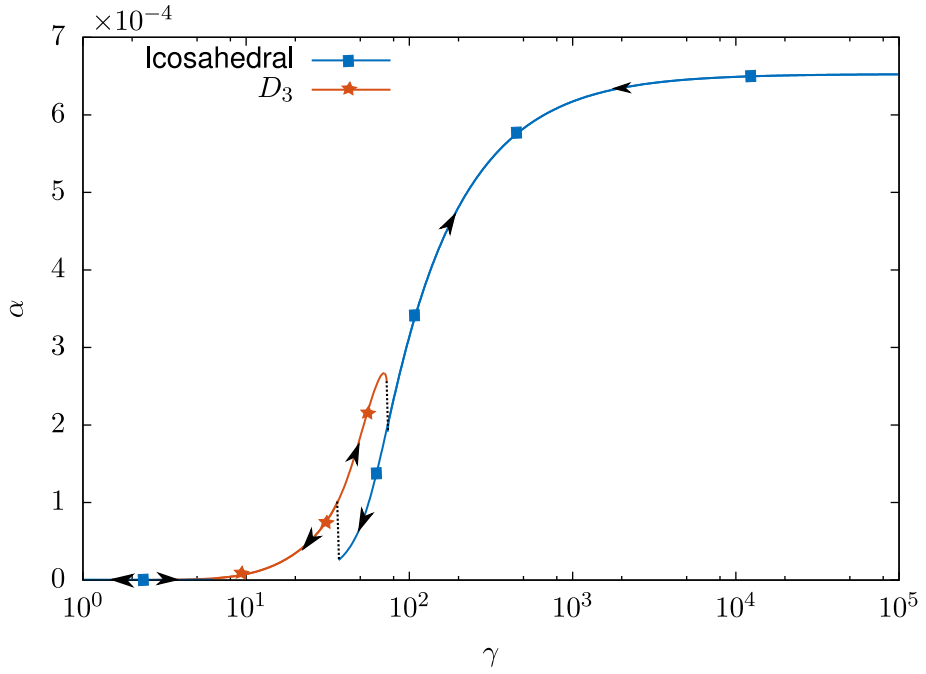

Figure 2.7: Asphericity $\alpha = \frac{<(R-R_0)^2>}{R_0^2}$ versus FvK number γ for $N = 72$ particles. The arrows indicate the direction of change of γ. Blue line: icosahedral symmetry. Orange line: D_3 symmetry. The dimensionless width of the Morse potential is $\delta = 0.09$.

The icosahedral symmetry of the initial structure was maintained down to $\gamma \simeq 36.4$. At $\gamma \simeq 36.4$ we encountered an abrupt increase in the asphericity while the symmetry changed from icosahedral to D_3 (with a single 3-fold axis and 3 two-fold axes perpendicular to the 3-fold axis). The D_3 symmetry persisted down to $\gamma \simeq 2.6$ where it reverted back to icosahedral. The energy differences between competing icosahedral and D_3 structures was of the order of 0.1 V_M, which was still significantly larger than our numerical error. When the FvK number was increased from 1 to 10^5 in 2000 log-scaled steps, the shell maintained icosahedral symmetry till $\gamma \simeq 6.3$ where it changed to D_3. D_3 symmetry was maintained till $\gamma \simeq 73.6$ when the shell reverted back to icosahedral symmetry. Icosahedral symmetry was then maintained for larger FvK numbers. Similar but smaller transitions were observed for $\delta = 0.10$.[1] The pattern of the inter-particle forces is shown in Figure 2.8 together with

[1]We chose to analyze the results obtained for $\delta = 0.09$ as the jumps in asphericity are larger than for the $\delta = 0.10$ case and the changes in bond stress patterns are easier to observe in Figure. 2.8. This was done as well for $N = 132$ and $N = 192$.

the shape of the shell for $N = 72$. The particles are located at the vertices of the triangular

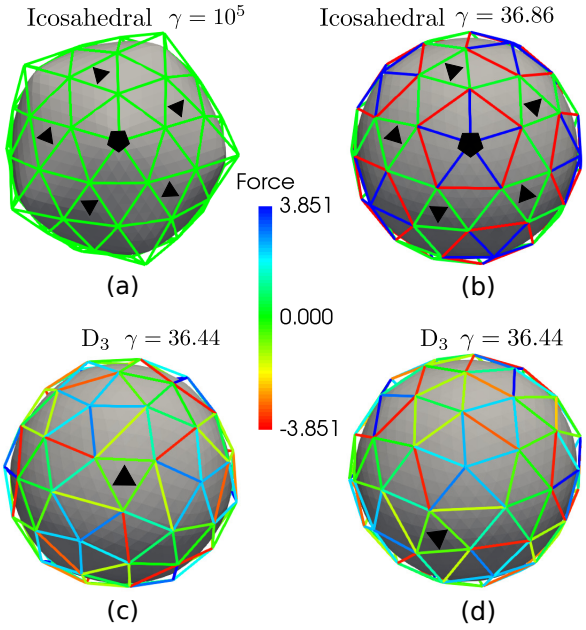

Figure 2.8: Shell shapes and inter-particle forces for $N = 72$, $\delta = 0.09$, and different FvK Number γ. Bonds shown in blue are under compression. Bonds shown in red are under tension. Bonds shown as green are under little or no stress. The C^1 surfaces spanned by the particles are shown in gray. The black markers indicate axis of symmetry. A pentagonal marker indicates a five-fold axis and a triangular marker denotes a three-fold axis.

network of bonds. The C^1 surface generated by the triangular network is shown in gray below the network. Note that the surface does not exactly interpolate between the particle locations since the Loop shell subdivision method used in this analysis is an approximating — not an interpolating — scheme. Inter-particle force levels are shown on a scale of -3.85 (tension) to $+3.85$ (compression) in units of V_M/r_e, which has been set to one. The lower limit of the tension level (-3.85) corresponds to the bond fracture limit. Figure 2.8 (a) and 2.8 (b) show two shells with icosahedral symmetry. The first is for large FvK numbers when the force levels are nearly zero, as expected for an isometric shell. The rounding of the C^1 surface at the 5-fold sites is due to the relative coarseness of a 72 node finite-element mesh. The FvK number of the shell in Figure 2.8 (b) is just above the instability point at $\gamma \simeq 36$. The elastic stress is focused at the twelve pentagonal pyramids, as expected

from continuum theory. Note that the pyramids are connected by stress-free bonds (green) so the stress pattern breaks up into twelve groups that are not exposed to external stress. This is what motivated the discussion of single pentagonal pyramids in Section 2.3. As in Section 2.3, the bonds along the perimeter of the pyramids are under tension while the bonds linking the central particle are under compression. The perimeter bonds are in fact practically at the fracture threshold of -3.85. This suggests that the instability of the $T = 7$ icosahedral state is in essence the soft-mode instability of Section 2.3. Figure 2.8 (c) and 2.8 (d) show two views of the shell with D_3 symmetry at $\gamma \simeq 36$, just below the instability point. Figure 2.8 (c) shows the shell along the single 3-fold axis and Figure 2.8 (d) shows the shell along the direction of the 5-fold axis of the former icosahedral structure. The new stress pattern is more uniform than that of the icosahedral shell: only two of the five bonds along the base of the deformed pyramids remain close to the fracture threshold. Between $\gamma \simeq 36$ and $\gamma \simeq 74$ icosahedral and D_3 states are both locally stable, which causes the hysteresis shown in Figure 2.7.

2.4.2 $N = 122$

The numerical studies of particle models restricted to spherical surfaces reported that structural instabilities become more noticeable with increasing shell radius [BGR03]. Figure 2.9 shows the dependence of the shape of a $N = 122$ shell as a function of γ, starting from a $T = 12$ CK icosahedral shell and with $\delta = 0.10$.

Though the $N = 122$ shell is a larger shell, we did not encounter structural instability. Figure 2.9 is consistent with continuum model [LMN03] except that the location of the buckling transition is about half smaller while the maximum amount of asphericity is about one third smaller. A change in the location of the buckling transition to larger or smaller γ values has been observed also for other discrete models [MRB10]. The reduction in value of asphericity is related to the rounding generated by the construction method for the C^1 surface with a small number of particles. The inset of Figure 2.9 shows the stress pattern at low FvK numbers. Note that the stress pattern is achiral, as expected for a $T = 12$

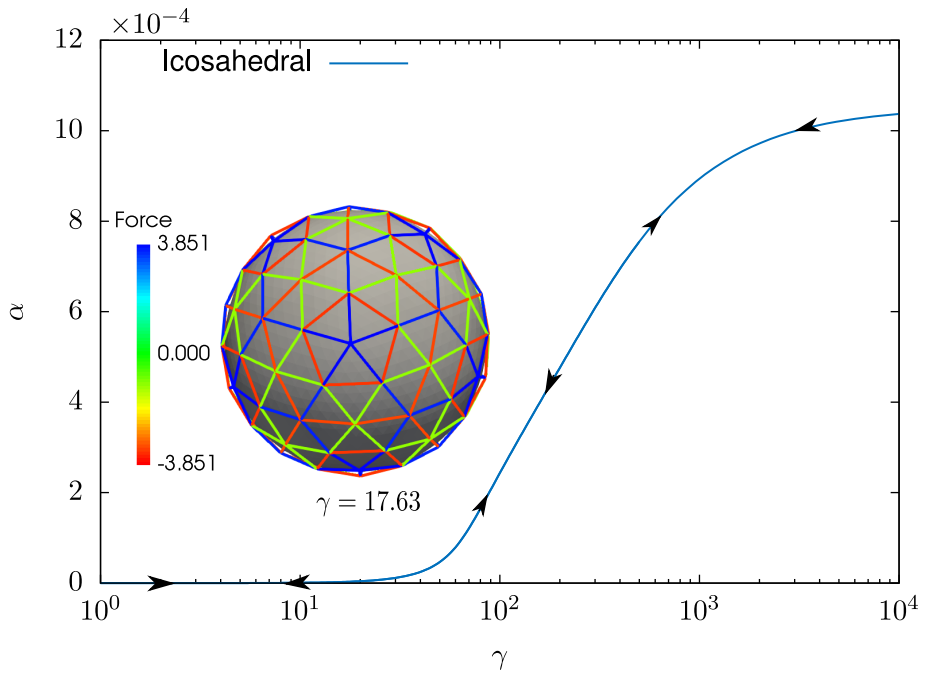

Figure 2.9: Asphericity $\alpha = \frac{<(R-R_0)^2>}{R_0^2}$ versus FvK number for $N = 122$ particles with $\delta = 0.10$. The inset shows the achiral bond pattern at a low FvK number viewed along a five-fold axis. In contrast to chiral shells (e.g., $N = 72, 132$, and 192), no instability is observed for $N = 122$ with $\delta = 0.10$.

shell. There is another distinct difference with the $N = 72$ stress pattern. The blue bonds radiating out from the 5-fold symmetry sites form a connected network that appears to be held in place by the overstretched red bonds along the base of the pyramids. The overall impression is that the shell is only barely stable. Indeed, when the dimensionless well width δ is reduced below 0.09 the $N = 122$ shell develops instability at low FvK numbers.

2.4.3 $N = 132$

Further increasing the number of particles, we considered next the case of $N = 132$ particles distributed on a $T = 13$ CK icosahedral shell. In this case we observe a discontinuity at $\gamma \simeq 71$ for decreasing FvK numbers and at $\gamma \simeq 124$ for increasing FvK numbers (Figure 2.10). There is an instability as well for $\delta = 0.10$ but the jump in asphericity has again a lower magnitude. Shell shapes and inter-particle forces for $N = 132$ are shown in Figure 2.11. The

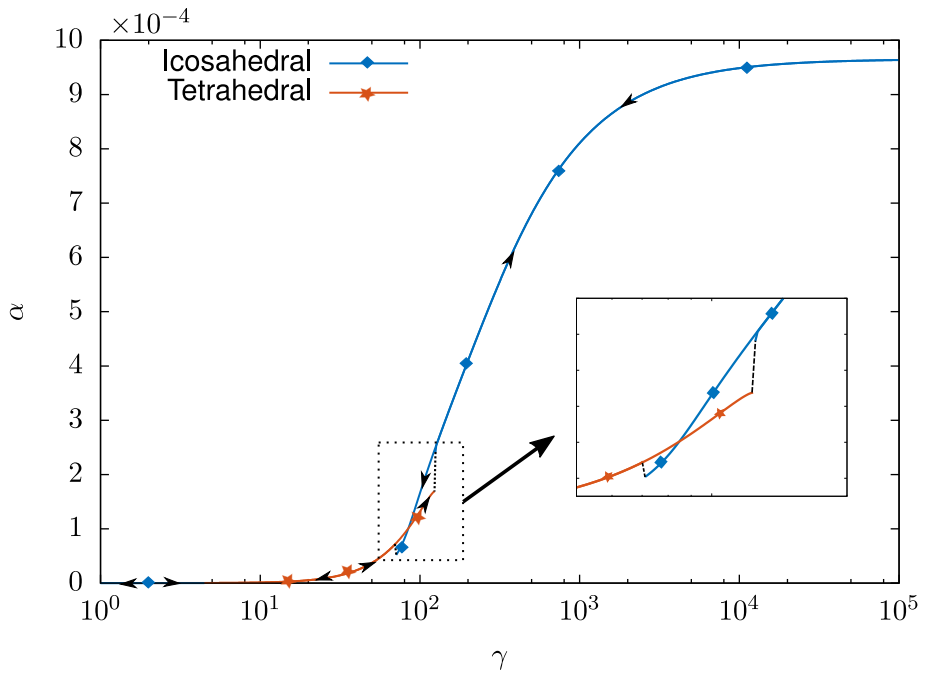

Figure 2.10: Asphericity versus versus FvK number γ for $N = 132$ with $\delta = 0.09$.

top row of Figure 2.11 shows two shells with icosahedral symmetry. The bond lengths in Figure 2.11 (a) with $\gamma = 10^5$ are — as expected — nearly at their equilibrium value. Note that the shell shape is now a closer approximation to an icosahedron than the corresponding case for $N = 72$. That is because a larger number of particles are used to generate the surface. The shell in Figure 2.11 (b) is poised near the instability at $\gamma \simeq 71$. The stress pattern of the twelve pyramids is similar to that of the $N = 72$ shell with the edge bonds of the pyramids at their fracture threshold. However, the pyramids are now linked by a network of (weakly) stressed bonds. The bottom row of Figure 2.11 shows the non-icosahedral shell just below the transition. It has *tetrahedral symmetry* with four three-fold symmetry axes. Figure 2.11 (c) shows a view along one of the three-fold axes while Figure 2.11 (d) shows a view along a former 5-fold symmetry axis. Note the relaxation of the edge bonds of the pyramids. The pattern of relaxed bonds of the distorted pyramid is different from that of the D_3 state for $N = 72$. If the FvK number is increased starting from $\gamma = 1$, then icosahedral symmetry is restored at $\gamma \simeq 124$. Similar transitions between icosahedral and tetrahedral symmetries at low FvK numbers are observed for $\delta = 0.10$.

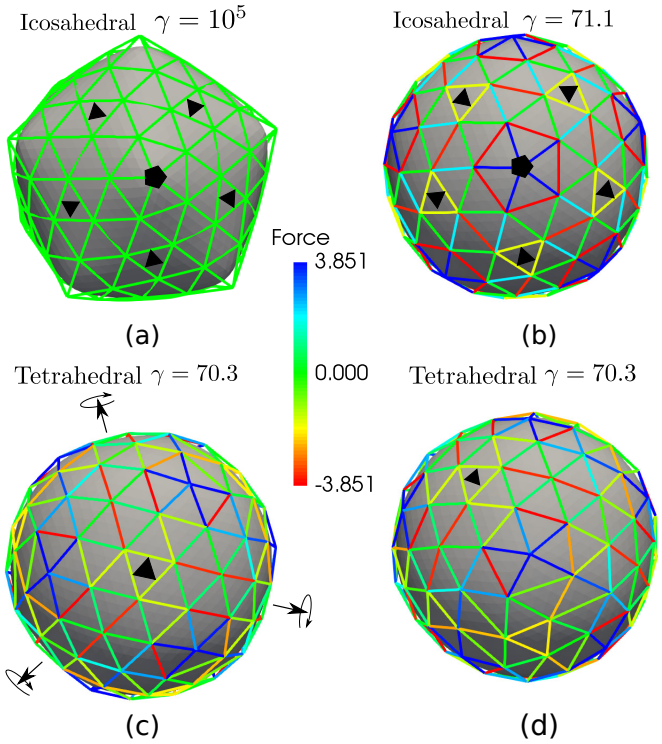

Figure 2.11: Shell shapes and inter-particle forces for $N = 132$ and $\delta = 0.09$. Unlike $N = 72$ case, for $N = 132$ we see transitions to tetrahedral shapes instead of D_3. The arrows in sub-figure (c) mark the remaining three-fold axis of tetrahedral symmetry, which are not visible when viewed along the three-fold axis marked with the black triangle.

2.4.4 $N = 192$

Continuing to increase the number of particles, at $N = 192$ we encounter an intricate sequence of instabilities. Figure 2.12 shows the corresponding asphericity plot, which presents noticeable discontinuities near $\gamma \simeq 69$ for decreasing FvK numbers and near $\gamma \simeq 131$ for increasing FvK numbers. The top row of Figure 2.13 shows icosahedral shells for large γ and for $\gamma \simeq 69$, i.e., just before the instability. At $\gamma \simeq 69$, the pentagonal pyramids are once again isolated stress units but now they are composed of *two* rings of bonds stretched to the fracture threshold. The bottom row in Figure 2.13 shows that just below the $\gamma \simeq 69$ instability, the shell has a D_3 structure. Strangely, when the FvK number was reduced further, the D_3 structure started to resemble the icosahedral structure just above the $\gamma \simeq 69$ instability. The D_3 structure transforms to a tetrahedral structure at $\gamma \simeq 3.5$. The sequence

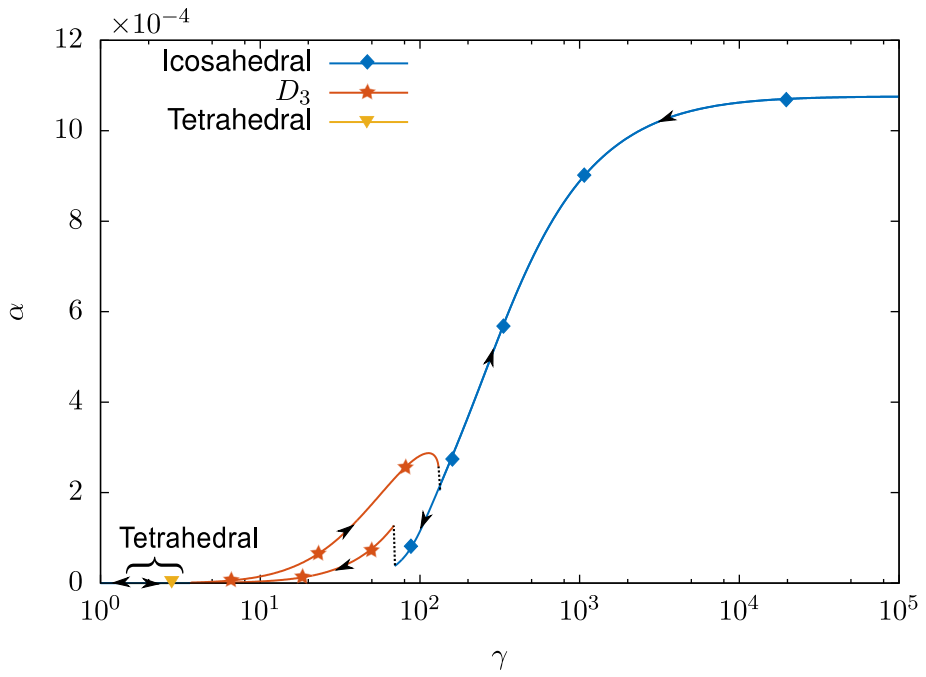

Figure 2.12: Asphericity α versus FvK number γ for $N = 192$ and $\delta = 0.09$. Instabilities at low FvK number result in the formation of shell shapes with D_3 as well as tetrahedral symmetries.

reverses if γ is increased.

2.4.5 Effect of Chirality

At $\delta = 0.1$, the $N = 122$ shell does not present a structural instability while the $N = 72, 132,$ and 192 shells show instabilities and discontinuities in the asphericity versus FvK plots. This finding indicates that an additional factor contributes to determining structural stability apart from the FvK number and the fracture strain δ. The $N = 72$, $N = 132$, and $N = 192$ shells have indeed an important feature in common — they are *chiral* — while $N = 122$ is not. This suggests that achiral shells are more stable than chiral shells. To investigate this aspect further we considered two additional achiral structures with $N = 92$ and $N = 162$. Figure 2.14 and Figure 2.15 show the asphericity α versus FvK number γ plots for $N = 92$ and $N = 162$ shells obtained with $\delta = 0.10$. For both cases, achiral Caspar-Klug structures with $T = 9$ (for $N = 92$) and $T = 16$ ($N = 162$) are formed at $\gamma = 10^5$. This icosahedral

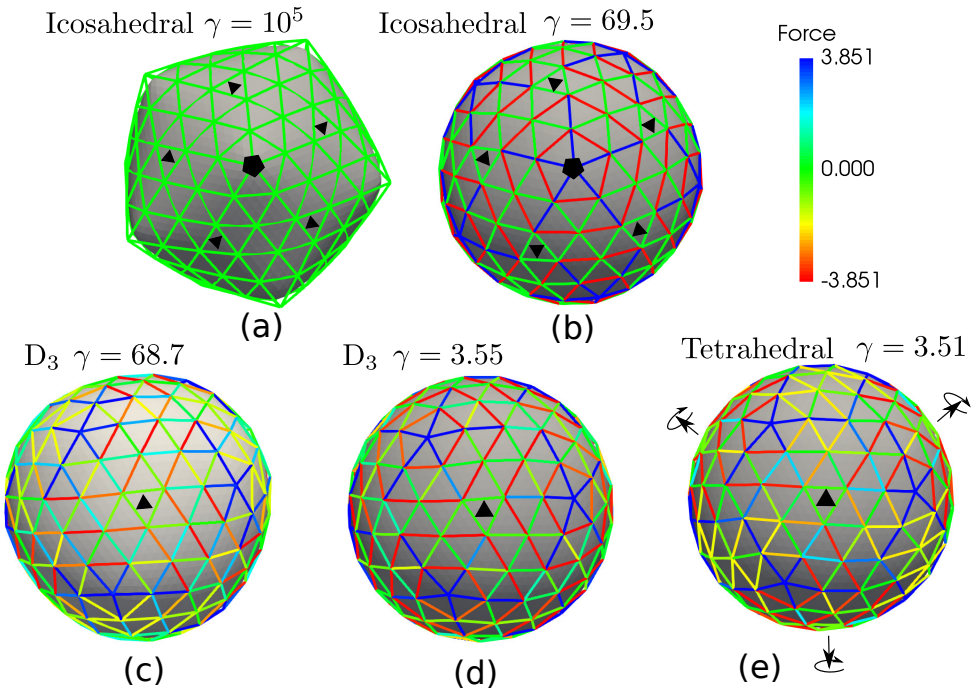

Figure 2.13: Shell shapes and inter-particle forces for $N = 192$ and $\delta = 0.09$. In this case, we observe transitions to both D_3 and tetrahedral states at low FvK numbers. Arrows in sub-figure (e) mark the three-fold axis of tetrahedral symmetry that are not visible. Similar structures are found for $\delta = 0.10$ as well.

symmetry is maintained at all values of FvK number, as in the case of $N = 122$ at $\delta = 0.10$.

Table 2.1 summarizes the critical delta values δ_c for chiral and achiral shells with different number of particles. All the achiral structures have a lower, although only slightly, values of δ_c.

2.5 Discussion

We have examined a simple model for protein shells assembled from disk-like components held together by weak bonds. The model combines the bonding description of earlier particle models with the bending energy of continuum elasticity theory. We used the model to evaluate the structural stability of icosahedral shells. For large FvK numbers the shells always have a well-defined icosahedral ground state when the number of particles N equals

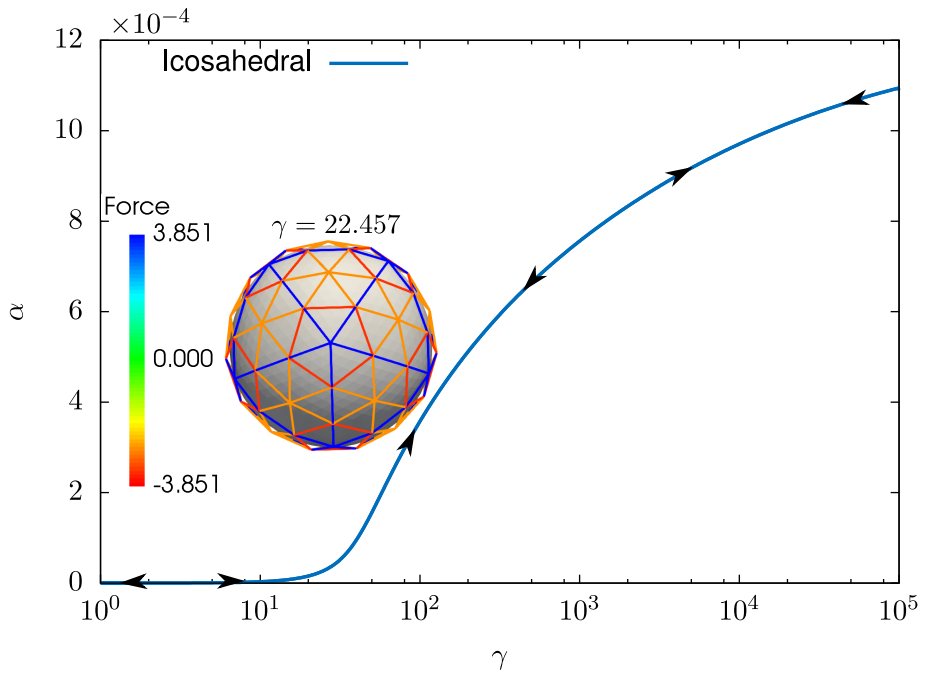

Figure 2.14: Asphericity $\alpha = \frac{<(R-R_0)^2>}{R_0^2}$ versus FvK number for $N = 92$ particles with $\delta = 0.10$. The inset show the $N = 92$ achiral structure with icosahedral symmetry at $\gamma = 22.5$. Icosahedral symmetry is stable for all values of γ at $\delta = 0.10$.

Table 2.1: Values of δ_c for different particle numbers N to show the effect of chirality

Number of particles	T number at $\gamma = 10^5$	Chirality	δ_c
72	7	Chiral	0.10
92	9	Achiral	0.09
122	12	Achiral	0.09
132	13	Chiral	0.10
162	16	Achiral	0.09
192	19	Chiral	0.10

$10T + 2$. At large FvK numbers, the nearest-neighbor particle separations are mostly close to the equilibrium spacing of the pair potential. As the FvK number is reduced, the shell undergoes a buckling transition consistent with continuum model. However, when the dimensionless width of the potential well, or equivalently, the fracture strain, is reduced below

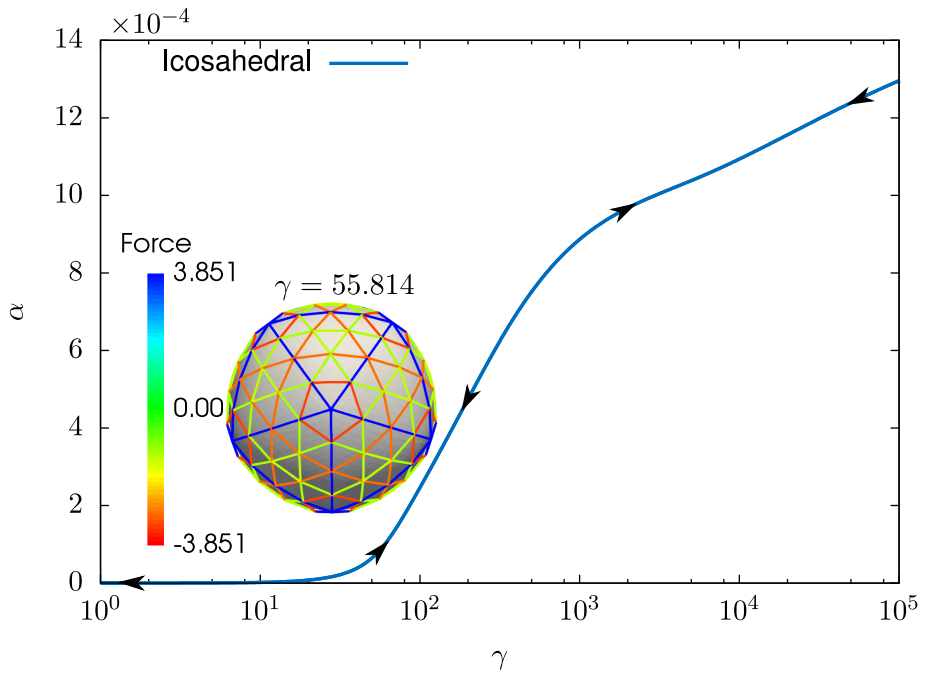

Figure 2.15: Asphericity $\alpha = \frac{<(R-R_0)^2>}{R_0^2}$ versus FvK number for $N = 162$ particles with $\delta = 0.10$. Inset shows the $N = 162$ achiral structure with icosahedral symmetry at $\gamma = 55.8$. At $\delta = 0.10$ the structure maintains icosahedral symmetry for all γ values.

a critical value, then the structure of the ground state is marked by a sequence of structural instabilities and symmetry changes in the region of the buckling transition. *Chiral* shells are found to be more prone to this instability. The depth of the Morse potential well represents the bonding strength between capsid proteins (5–7 k_BT [CZ02]). The equilibrium separation of the potential corresponds to the diameter of a disk ($\simeq$ 10 nm) while the width of the potential well corresponds to the typical range of the hydrophobic interaction in proteins (0.4–1.0 nm [OPP14]). The estimated fracture strain of a surface composed of protein shells is in the range $0.04 - 0.10$ using these values. This is (just) below the critical fracture strain. That means that large protein shells indeed should be expected to develop structural instability for FvK numbers below the buckling transition. However, large viral capsids [BOF99] are observed to be stable. We conclude that the self-assembly of large, structurally stable protein shell is possible only if the FvK number of the assembled shell is well above the buckling threshold. The observation that large viral shells indeed are buckled [LMN03, BOF99]

is consistent with this conclusion. Another piece of supporting evidence is that molecular modeling studies of deformed viral shells [ARW09] indicate that viral capsids deformed by more than ten percent are subject to *rebonding*, which means that bonds between capsid protein have been overstretched. Rebonding is probably the origin of hysteresis observed in AFM studies of viral shells [RBW10].

A number of caveats in our model should be noted. We treated the capsomers as identical particles. In actuality, one should distinguish pentamers from hexamers. Fine-tuning of the pair interaction by distinguishing hexamer-hexamer, hexamer-pentamer, and pentamer-pentamer interaction is possible. It was found that this does stabilize icosahedral shells on spherical surfaces [ZRB04]. However, fine-tuning barely stabilizes icosahedral shells for $N = 72$ particles and we believe — but have not checked — that fine-tuning cannot stabilize any larger icosahedral shells. Next, the energy differences between the icosahedral, D_3, and tetrahedral states are small. For example, for $N = 72$ at $\gamma = 50.9$ both icosahedral and D_3 structures co-exist (Figure 2.7). The energies of these two structures differ by 0.16 Y_M. In the case of $N = 132$ at $\gamma = 100.5$ the difference between tetrahedral and icosahedral co-existing structures (Figure 2.11) is 2.2 Y_M. In the case of $N = 192$ the difference between D_3 and icosahedral structures at $\gamma = 100.5$ (Figure 2.12) is 1.7 Y_M. These energy differences are close to, or less than, the energy associated with thermal fluctuations. This means that *thermal fluctuations* cannot be neglected and that free energy differences should be computed instead of differences in elastic energy of these structures. We are in the process of including thermal fluctuations in our studies of shells using particle models. Given the quasi-degeneracy of the low-lying energy states it seems likely that for low FvK numbers, shells might be in a *liquid-like* state when thermal fluctuations are included.

Finally, as mentioned, the molecular modeling calculations on deformed capsids indicate a possibly important role for rebonding. The numerical method used in this paper did not allow for rebonding: the topology of the network pattern of bonds introduced for the large FvK isometric shells was maintained for smaller FvK numbers, though we did allow changes in symmetry. In the next chapter, we will extend our numerical methods to include rebonding, and a fully discrete model where the bending deformations are described using

discrete angles between outward normals of adjacent capsomers.

CHAPTER 3

Oriented Particles Shell Model

The continuum and the hybrid models discussed in Chapter 1 and Chapter 2 are both zero temperature models. In the literature, there are examples of studies of thermal fluctuations on shells [PKW16, GKH18, KN17, PVG12, PM98]. Paquay *et al* [PKW16] have reported that an icosahedral packing on a rigid spherical surface is very susceptible to thermal fluctuations. Pérez-Garrido *et al* [PM98] have simulated melting of particles on a rigid sphere whereas Guerra *et al* [GKH18] investigate freezing on a sphere. All of these works assume rigid surfaces. Paulose *et al* and Košmrlj *et al* [PVG12, KN17] have used a deformable shell but their model is a continuum model and therefore works only for a large number of particles and the particles are assumed to be glued to the surface. This model cannot be used to study melting as it does not allow bond-rearrangements. Further, they assume an amorphous shell i.e. because of the large number of particles they neglect the effect of disclinations and dislocations on the shell. Thus, the discrete model that we present in this chapter is unique because it models a finite deformable shell which allows bond rearrangements.

In next sections we will introduce the model including the discrete bending potentials, an estimate for a FvK number for this model and a variational form of Brownian dynamics equation which we will use for numerical simulations. In Section 3.2.3 we will report the results from numerical simulations.

3.1 The Discrete Model

The continuum and hybrid models have a predefined surface which is discretized to form a finite element mesh. This poses a challenge for introducing thermal fluctuations because

we will have to dynamically remesh the surface to accommodate bond-rearrangements. We circumvent this problem by not using any surface. Instead, we will use a cloud of *oriented particles* [ST92] which interact via special potentials that prefer to arrange the particles as a surface instead of a cluster. Such a point cloud is called an oriented particle system (OPS). Every oriented particle has six degrees of freedom — three positional degrees of freedom and three orientational degrees of freedom. Instead of storing the orientations as a unit normal in a global coordinate system, we will store these as rotation vectors which are products of the angles and the axis vectors required to rotate the z axis of the global coordinate system to the orientation of the particles. Figure 3.1 shows a typical OPS for our problem.

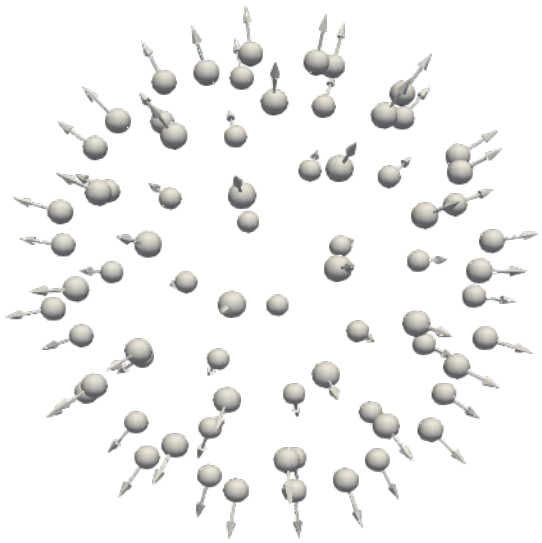

Figure 3.1: A typical oriented particle system that we investigate looks like a spherical point cloud where each point has an associated orientation.

3.1.1 Oriented Particles System Potentials

The OPS potentials consist of two parts. The Morse potential is used to control average spacing between the particles. The *Co-normality* and *Co-circularity* potentials arrange the particles in the form of a surface rather than a 3D cluster. Thus, these two potentials serve

as discrete bending potentials. The Morse potential is the same as in Chapter 2

$$\phi_M = V_M \sum_{i \neq j} \left(e^{-2a(|\mathbf{r}_{ij}|-r_e)} - 2e^{-a(|\mathbf{r}_{ij}|-r_e)} \right) \tag{3.1}$$

The co-normality potential is

$$\phi_N = K \sum_{i \neq j} |\mathbf{n_i} - \mathbf{n_j}|^2. \tag{3.2}$$

It tries to align the orientations of two interacting particles such that they are either parallel or anti-parallel. Figure 3.2 shows the effect of this potential. The co-circularity potential is

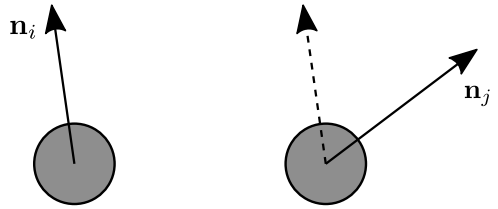

Figure 3.2: Co-normality potential has minimum energy when the orientations of the two interacting particles are parallel or anti-parallel to each other. The solid arrows represent the original orientations and the dashed arrow indicates the minimizing orientation.

defined as

$$\phi_C = K \sum_{i \neq j} \left(\frac{(\mathbf{n_i} + \mathbf{n_j}) \cdot \mathbf{r_{ij}}}{|\mathbf{r_{ij}}|} \right)^2. \tag{3.3}$$

This potential has a minimum energy when the components of the orientations of two interacting particles along the direction joining the two particles are equal and opposite. Figure 3.3 shows the effect of co-circularity potential on orientation of a neighboring particle. Therefore, the total potential energy of a cloud of oriented particles is

$$E = \phi_M + \phi_N + \phi_C \tag{3.4}$$

For numerical simulations, we also need to calculate derivatives of these potentials with respect to $\mathbf{r}^{(n+1)}$ and the rotation vectors associated with the particles. These calculations have been shown in Appendix A.

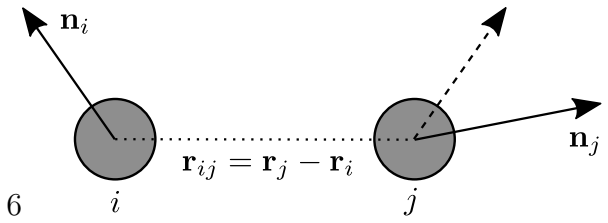

Figure 3.3: Co-circularity potential has minimum energy when the orientations are mirror images of each other. The solid lines denote the original orientations and the dashed line denotes the minimizing orientation.

3.1.2 The Brownian Dynamics Equations

We want to include temperature effects through Brownian motion. On the lines of Ermak-McCammon [EM78] formulation, we can write Brownian dynamics force balance as

$$\frac{\partial E}{\partial \mathbf{r}_i^{n+1}} + \frac{k_B T}{D_r} \frac{\mathbf{r}_i^{(n+1)} - \mathbf{r}_i^{(n)}}{\Delta t} - k_B T \sqrt{\frac{2}{D_r \Delta t}} \boldsymbol{\xi}_{r_i} = 0, \tag{3.5}$$

$$\frac{\partial E}{\partial \mathbf{n}_i^{n+1}} + \cancel{\frac{k_B T}{D_n}} \frac{\mathbf{n}_i^{(n+1)} - \mathbf{n}_i^{(n)}}{\Delta t} - \cancel{k_B T \sqrt{\frac{2}{D_n \Delta t}} \boldsymbol{\xi}_{n_i}} = 0 \tag{3.6}$$

where D_r and D_n are the diffusion coefficients for position degrees of freedom $\mathbf{r}_i$ and orientation degrees of freedom $\mathbf{n}_i$ respectively. $\boldsymbol{\xi}$'s are random vectors whose components are drawn from a normal distribution with mean 0 and standard deviation 1. In our model we assume that $D_n >> D_r$ and $D_n \to \infty$. We can make this assumption because the position degrees of freedom form part of conservation of mass through

$$\int \rho\left(\mathbf{r} - \mathbf{r}_i\right) \mathrm{d}V = N \tag{3.7}$$

where N is number of particles. Hence, particles cannot 'teleport' from one location to another without passing through all intermediate position values. This makes changes in position degrees of freedom slower than the orientation degrees of freedom. This helps us get rid of the last two terms in the force balance for orientation degrees of freedom. Thus the rate of diffusion for position degrees of freedom is much slower than that for orientation degrees of freedom.

It is important to note that the Equation 3.6 is not mathematically correct because $\mathbf{n_i}$

and $\mathbf{n_j}$ are unit normals and the solutions of Equation 3.6 are not guaranteed to be unit normals. One can add constraint force equations for each orientation in the system that the sum of their components adds up to unity. But this increases the computational complexity by a lot. Hence, we store the orientational information as rotation vectors which map the z-direction of the global coordinate system to the orientations. Rotation vectors do not require any constraints.

3.1.3 Variational Formulation

We will reformulate Equations 3.5 and 3.6 as a minimization problem. This will enable us to use the Limited memory BFGS [ZBL97] algorithm that we used for solving the hybrid model. We do this because the computer program for this solver is already available to us from our previous work. So will construct a functional whose Euler-Lagrange equations will give us Equation 3.5 and Equation 3.6.

Consider

$$\begin{aligned} I'[\mathbf{r}^{(n+1)}, \mathbf{n}^{(n+1)}] = V_M \sum_{i \neq j} \left(e^{-2a(|\mathbf{r}_{ij}|-r_e)} - 2e^{-a(|\mathbf{r}_{ij}|-r_e)} \right) \\ + K \sum_{i \neq j} |\mathbf{n}_i - \mathbf{n}_j|^2 + K \sum_{i \neq j} \left(\frac{(\mathbf{n}_i + \mathbf{n}_j) \cdot \mathbf{r}_{ij}}{|\mathbf{r}_{ij}|} \right)^2 \\ + \left(\frac{k_B T}{D_r \Delta t} \right) \frac{\left(\mathbf{r}^{(n+1)} - \mathbf{r}^{(n)} \right)^2}{2} - k_B T \sqrt{\frac{2}{D_r \Delta t}} \boldsymbol{\xi}_r \cdot \left(\mathbf{r}^{(n+1)} - \mathbf{r}^{(n)} \right). \end{aligned} \tag{3.8}$$

where the superscripts $(n+1)$ and (n) denote time-steps. The diffusion coefficient D_r is a function of temperature as

$$D_r = \mu \, k_B \, T \tag{3.9}$$

where μ is a temperature independent "mobility". Using this equation we can rearrange the

functional into following form

$$
\begin{aligned}
I'[\mathbf{r}^{(n+1)}, \mathbf{n}^{(n+1)}] = V_M \sum_{i \neq j} \left(e^{-2a(|\mathbf{r}_{ij}|-r_e)} - 2e^{-a(|\mathbf{r}_{ij}|-r_e)} \right) \\
+ K \sum_{i \neq j} |\mathbf{n}_i - \mathbf{n}_j|^2 + K \sum_{i \neq j} \left(\frac{(\mathbf{n}_i + \mathbf{n}_j) \cdot \mathbf{r}_{ij}}{|\mathbf{r}_{ij}|} \right)^2 \\
+ \left(\frac{1}{\mu \Delta t} \right) \frac{\left(\mathbf{r}^{(n+1)} - \mathbf{r}^{(n)} \right)^2}{2} - \sqrt{\frac{2k_B T}{\mu \Delta t}} \boldsymbol{\xi}_r \cdot \left(\mathbf{r}^{(n+1)} - \mathbf{r}^{(n)} \right).
\end{aligned}
\tag{3.10}
$$

Let us use the following substitutions,

$$
\begin{aligned}
\alpha &= \frac{r_e^2}{V_M} \frac{1}{\mu \Delta t}, \\
\beta &= \frac{V_M}{k_B T}, \\
\gamma &= \frac{4a^2 R^2 V_M}{\sqrt{3} K}.
\end{aligned}
\tag{3.11}
$$

R is the zero temperature radius of the shell. Equation for the FvK number γ will be derived in Section 3.1.5. β is a non-dimensional measure of temperature expressed relative to the Morse potential equilibrium energy. α controls the viscosity and size of the time step. In Section 3.1.6 we will see how to choose the parameters α and β for our analysis. Now we can write

$$
\begin{aligned}
I'[\mathbf{r}^{(n+1)}, \mathbf{n}^{(n+1)}] = V_M \sum_{i \neq j} \left(e^{-2a(|\mathbf{r}_{ij}|-r_e)} - 2e^{-a(|\mathbf{r}_{ij}|-r_e)} \right) \\
+ \frac{4a^2 R^2}{\sqrt{3}} \frac{V_M}{\gamma} \left(\sum_{i \neq j} |\mathbf{n}_i - \mathbf{n}_j|^2 + \sum_{i \neq j} \left(\frac{(\mathbf{n}_i + \mathbf{n}_j) \cdot \mathbf{r}_{ij}}{|\mathbf{r}_{ij}|} \right)^2 \right) \\
+ \frac{\alpha V_M}{r_e^2} \frac{\left(\mathbf{r}^{(n+1)} - \mathbf{r}^{(n)} \right)^2}{2} - \frac{V_M}{r_e} \sqrt{\frac{2\alpha}{\beta}} \hat{\boldsymbol{\xi}}_r \cdot \left(\mathbf{r}^{(n+1)} - \mathbf{r}^{(n)} \right).
\end{aligned}
\tag{3.12}
$$

We can divide the above equation throughout by V_M to get a non-dimensional equation as

follows:

$$
\begin{aligned}
I[\mathbf{r}^{(n+1)}, \mathbf{n}^{(n+1)}] = & \sum_{i \neq j} \left(e^{-2a(|\mathbf{r}_{ij}|-r_e)} - 2e^{-a(|\mathbf{r}_{ij}|-r_e)} \right) \\
& + \frac{4a^2R^2}{\sqrt{3}\gamma} \left(\sum_{i \neq j} |\mathbf{n}_i - \mathbf{n}_j|^2 + \sum_{i \neq j} \left(\frac{(\mathbf{n}_i + \mathbf{n}_j) \cdot \mathbf{r}_{ij}}{|\mathbf{r}_{ij}|} \right)^2 \right) \\
& + \frac{\alpha}{r_e^2} \frac{\left(\mathbf{r}^{(n+1)} - \mathbf{r}^{(n)} \right)^2}{2} - \frac{1}{r_e} \sqrt{\frac{2\alpha}{\beta}} \hat{\boldsymbol{\xi}}_r \cdot \left(\mathbf{r}^{(n+1)} - \mathbf{r}^{(n)} \right).
\end{aligned} \tag{3.13}
$$

When we evolve the OPS shell in time, there are rigid body motions due to thermal fluctuations. We compensate for the rigid body translations by subtracting the mean of all particle positions from each particle position at every time step. We get rid of the rigid rotations using Kabsch algorithm [Kab76].

3.1.4 Area Constraint

If we try to minimize Equation 3.13 as it is and evolve the system in time, we will find that on heating the particles diffuse away from each other and the shell *evaporates*. This is unphysical for a viral shell. Further, the proteins that form the shell of a virus do not stretch much. Hence, it is fair to assume that the total surface area of the shell is fixed. We will apply the area constraint using Augmented-Lagrangian (AL) technique.

Our optimization problem from Equation 3.13 is

$$
\begin{aligned}
& \min_{\mathbf{r}^{(n+1)}, \mathbf{n}^{(n+1)}} I[\mathbf{r}^{(n+1)}, \mathbf{n}^{(n+1)}] \\
& \text{subject to} \quad A\left(\mathbf{r}^{(n+1)}\right) - A_0 = 0
\end{aligned}
$$

where A_0 is the zero-temperature area and $A\left(\mathbf{r}^{(n+1)}\right)$ is the area after $n+1$ time steps. We can convert this problem into an unconstrained minimization problem by adding a Lagrange multiplier term and an augmenting penalty term as follows

$$
F[\mathbf{r}^{(n+1)}, \mathbf{n}^{(n+1)}] = I[\mathbf{r}^{(n+1)}, \mathbf{n}^{(n+1)}] + \frac{k^{(n+1)}}{2} \left(A^{(n+1)} - A_0 \right)^2 - \lambda^{(n+1)} \left(A^{(n+1)} - A_0 \right) \tag{3.14}
$$

where $k^{(n+1)}$ is a spring constant of the penalty term at time step $n+1$ and $\lambda^{(n+1)}$ is an

estimate of the Lagrange multiplier. The algorithm of AL method that we use at *each time step* in our numerical simulations is as follows:

1. Set $k^{(n+1)} = 1000.0$ and $\lambda^{(n+1)} = 10.0$.
2. Find $\mathbf{r}^{(n+1)}, \mathbf{n}^{(n+1)} = \text{argmin } F[\mathbf{r}^{(n+1)}, \mathbf{n}^{(n+1)}]$
3. While $\left(A^{(n+1)} - A_0\right) > 10^{-8}$, repeat
   (a) $\lambda^{(n+1)} \leftarrow \lambda^{(n+1)} - k^{(n+1)}\left(A^{(n+1)} - A_0\right)$
   (b) $k^{(n+1)} \leftarrow 10 \times k^{(n+1)}$
   (c) Find $\mathbf{r}^{(n+1)}, \mathbf{n}^{(n+1)} = \text{argmin } F[\mathbf{r}^{(n+1)}, \mathbf{n}^{(n+1)}]$

At the end of this procedure the area constraint is satisfied to a desired tolerance. The advantage of Augmented Lagrangian method over penalty method is that $k^{(n+1)}$ does not need to go to infinity and thus ill-conditioning is avoided. The advantage of Augmented Lagrangian method over method of Lagrange multipliers is that we do not introduce an extra degree of freedom in our system because the Augmented Lagrangian parameters k and λ are solved for iteratively in an external loop.

3.1.5 FvK number of OPS Potentials

The FvK number is an important parameter of our problem. We need to find an expression for FvK number for the OPS potentials. We need to find an effective bending modulus for the co-normality and co-circularity potential. We will do this by comparing the bending energies of a flat plate of hexagonal lattice with that of the same plate rolled into a cylinder.

Let's consider a flat plate of particles arranged on a triangular lattice interacting via Morse potential with equilibrium spacing r_e. Figure 3.4 shows a lattice with $W = 20$ bonds along the horizontal direction. We will call the vertical dimension of this strip as $H = 1$ unit. We can construct longer cylinders by combining multiple such strips along the vertical direction of the plate. As the point normals are pointing radially outwards, co-circularity

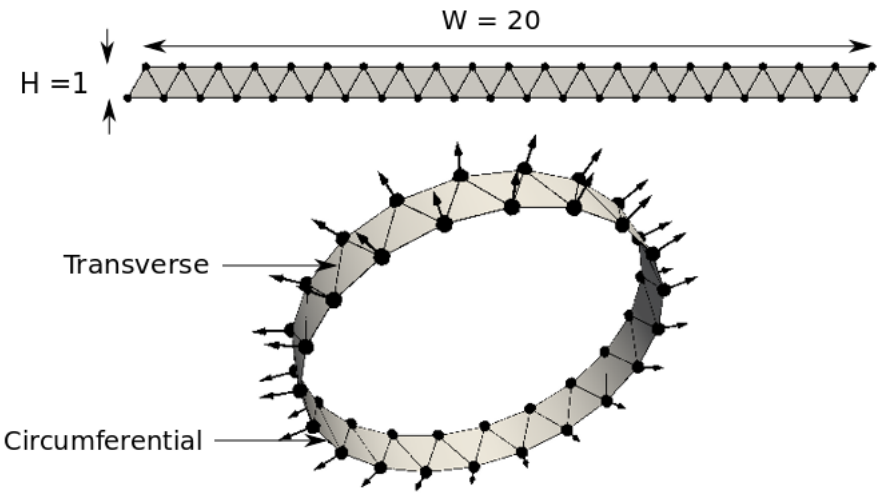

Figure 3.4: This figure shows formation of a bucky tube from a flat plate with triangular lattice. There are two types of bonds in the tube – circumferential and transverse.

potential

$$\phi_C = K \sum_{i \neq j} \left(\frac{(\mathbf{n_i} + \mathbf{n_j}) \cdot \mathbf{r_{ij}}}{|\mathbf{r_{ij}}|} \right)^2 = 0.$$

Since the lattice spacing of the plate and the tube are equal the Morse potential energies of both the structures are equal. Thus, the only difference in the energies of these two structures is due to the co-normality potential

$$\phi_N = K \sum_{i \neq j} |\mathbf{n_i} - \mathbf{n_j}|^2$$

There are two types of bonds in the tube as shown in Figure 3.4 – transverse bonds and circumferential bonds. For a circumferential bond we can show that

$$|\mathbf{n_1} - \mathbf{n_2}|^2 = 2 \left(1 - \cos \left(\frac{2\pi}{W} \right) \right)$$

For a transverse bond, we have

$$|\mathbf{n_1} - \mathbf{n_2}|^2 = 2 \left(1 - \cos \left(\frac{\pi}{W} \right) \right)$$

The number of transverse bonds in the tube is $W(H+1)$. The number of circumferential

bonds is $2WH$. Thus, the total co-normality energy is

$$\phi_N = 2KW\left[3H + 1 - 2H\cos\left(\frac{\pi}{W}\right) - (H+1)\cos\left(\frac{2\pi}{W}\right)\right]. \tag{3.15}$$

Bending energy of a cylinder with length L is $(\kappa\pi L)/R$. Comparing this with the equation for ϕ_N above, using $L = H\sqrt{3}/2$, and $R = W/2\pi$ we get

$$\kappa = \frac{2K}{\sqrt{3}H}\frac{W^2}{\pi^2}\left[3H + 1 - 2H\cos\left(\frac{\pi}{W}\right) - (H+1)\cos\left(\frac{2\pi}{W}\right)\right] \tag{3.16}$$

Assuming small angles, we can use Taylor's series expansion

$$\cos(x) = 1 - \frac{x^2}{2} + \ldots$$

to simplify the above equation to

$$\kappa = K\frac{6H+4}{\sqrt{3}H} \tag{3.17}$$

From this, we conclude that κ and K differ only by a factor for the case of a cylinder. For our calculations on a sphere, for simplicity, we will assume $K \approx \kappa$. The two-dimensional Young's modulus for Morse potential is

$$Y_{2D} = \frac{4a^2V_M}{\sqrt{3}} \tag{3.18}$$

Therefore, the Föppl von Kármán number can be written as

$$\gamma = \frac{Y_{2D}R^2}{\kappa} = \frac{4a^2V_MR^2}{\sqrt{3}K} \tag{3.19}$$

3.1.6 Choosing Parameters α and β

We can calculate the diffusion coefficient in terms of α and β as

$$D_r = \frac{r_e^2}{\alpha\beta\Delta t}.$$

The diffusion coefficient can also be obtained from slope of a $\langle r^2\rangle$ versus time plot.

$$D_r = \frac{\langle r^2\rangle_2 - \langle r^2\rangle_1}{t_2 - t_1}$$

where $\langle r^2 \rangle$ is the mean squared displacement of particles of the shell and t is simulation time. Assuming that

$$\langle r^2 \rangle_2 - \langle r^2 \rangle_1 = p^2 \, r_e^2 \quad \text{where } p \text{ is } \mathcal{O}(1) \text{ and}$$
$$t_2 - t_1 = \Delta t \, N$$

where Δt is simulation time-step size and N is the number of time steps we can write

$$\alpha = \frac{N}{\beta p^2}$$

As an example, if we are interested in the range of β from 1 to 10, if we use $N = 10^5$ time-steps and $p = 2$ then we should set α in the range 2.5×10^4 to 2.5×10^3.

3.2 Thermal Response of Finite Deformable Shells

In this section, we discuss two different effects of heating on the shell as a function of the FvK number. At FvK numbers below the zero temperature buckling transition heating the shell causes it to melt. At higher FvK numbers heating causes the shell to crumple.

3.2.1 Melting

To identify the melting temperature of the shell, we calculate relative neighbor-neighbor displacement [BGL85] of every particle at every time step. Then we calculate a mean squared displacement (MSD) for the entire shell for the current time step. We can plot MSD versus time for different temperatures at the same FvK number. For a molten shell, MSD will go on increasing linearly as a function of time. Of course, for very large times MSD will saturate because the shell has a limited surface area and two particles that were initially nearest neighbors can be separated by diameter of the shell at maximum. Figure 3.5 shows a MSD versus time plot for $\gamma = 0.1$ and various values of β. We can calculate the slope of MSD vs time plot for each temperature. Physically, the slope gives the diffusion coefficient. For a molten structure diffusion coefficient increases linearly with temperature. By finding the temperature at which the diffusion coefficient versus temperature line intersects the

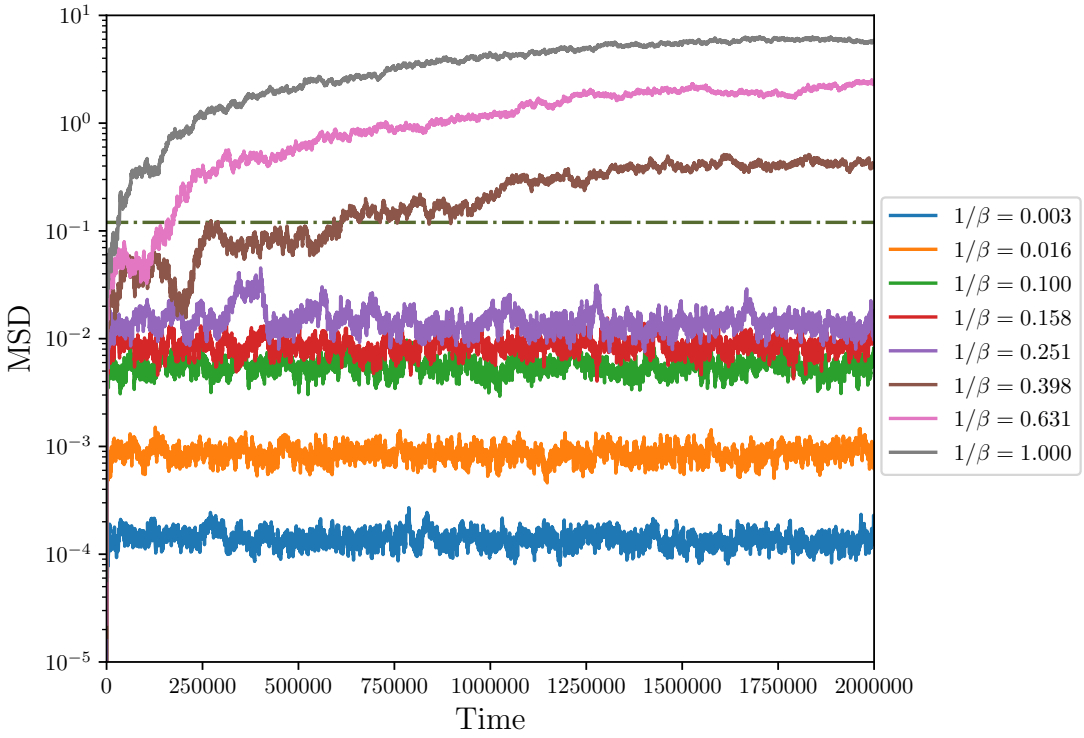

Figure 3.5: Mean squared displacement as a function of time for $\gamma = 25.46$ for various temperatures for a $T = 7$ structure. The dash-dot line marks the Lindemann criterion of 0.12 [BGL85] for a Lennard-Jones crystal. For very low temperatures the MSD fluctuates about a mean value for all times. For molten structures, the MSD rises quickly, crosses the Lindemann criterion mark and eventually saturates

temperature axis we can determine the melting temperature. Figure 3.6 shows a sample plot for $\gamma = 25.46$ for $T = 7$ structure.

Visualizations of the oriented partciles on a shell at a low FvK number but a temperature above the corresponding melting temperature have been shown in Figure 3.7. In subfigure (a), the particles at time step 1 have been shown. This structure has its icosahedral symmetry almost intact as the particles have not diffused very far from their initial positions. In subfigure (b), the particles have diffused far from their original positions and the icosahedral symmetry is visibly lost.

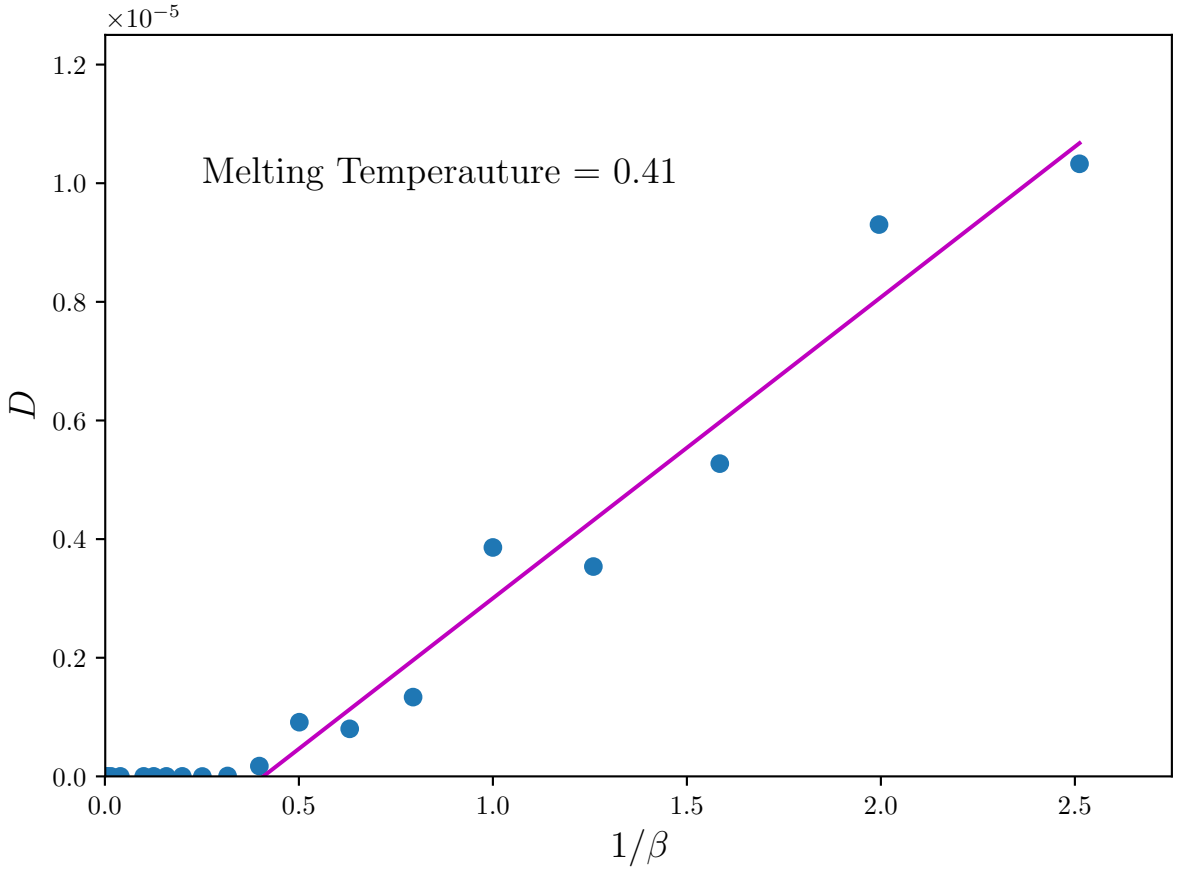

Figure 3.6: Diffusion coefficients have been plotted as a function of temperatures for $\gamma = 25.46$. After the melting, diffusion coefficients rise linearly with temperature. The magenta line is obtained by fitting a straight line through the scatter plot excluding the values which are almost zero.

3.2.2 Roughening

Paulose *et al* [PVG12] and Košmrlj *et al* [KN17] have reported on statistical mechanics of thin solid shells. They report that thermal fluctuations increase the effective bending rigidity of the shell and decrease their effective 2D Young's modulus. They also generate an effective external pressure on the shell. One of their results that is relevant for us is

$$R_{\max} \approx 160 \frac{\kappa_0}{k_B T} \sqrt{\frac{\kappa_0}{Y_0}} \tag{3.20}$$

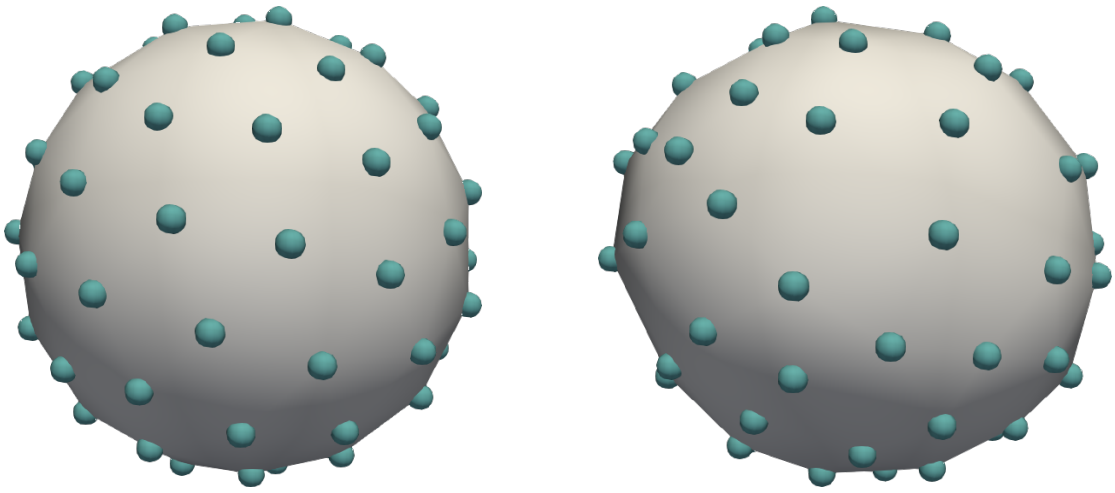

(a) t = 1 (b) t = 2000000

Figure 3.7: Visualization of oriented particles for $\gamma = 10.18$ and $1/\beta = 1.995$ at different time steps t. As time progresses the particles flow past each other and the positional order is lost.

where κ_0 and Y_0 are zero temperature bending and 2D Young's modulus and $R_{\max}$ is the largest shell which is stable against crumpling by the effective external pressure due to temperature T. We performed numerical simulations only for the same shell at different temperatures. Therefore, we can invert Equation 3.20 to write the temperature at which we can expect a shell of a given radius to buckle due to pressure as

$$\frac{1}{\beta} \approx \frac{640}{\sqrt{3}} a^2 R^2 \gamma^{-3/2} \tag{3.21}$$

To determine the temperature at which crumpling begins for a particular FvK number, we look at the volume of the shell as a function of time. For a solid structure the volume fluctuates about a mean value whereas for a crumpled structure the slope of volume versus time plot becomes negative. Figure 3.8 shows the volume vs temperature plots for various temperatures at FvK number 2541.1.

Visualizations of shell at a high FvK number have been shown in Figure 3.9. Initially, the structure resembles the zero temperature form. But as time progresses due to the effective thermal pressure, the surface becomes crumpled.

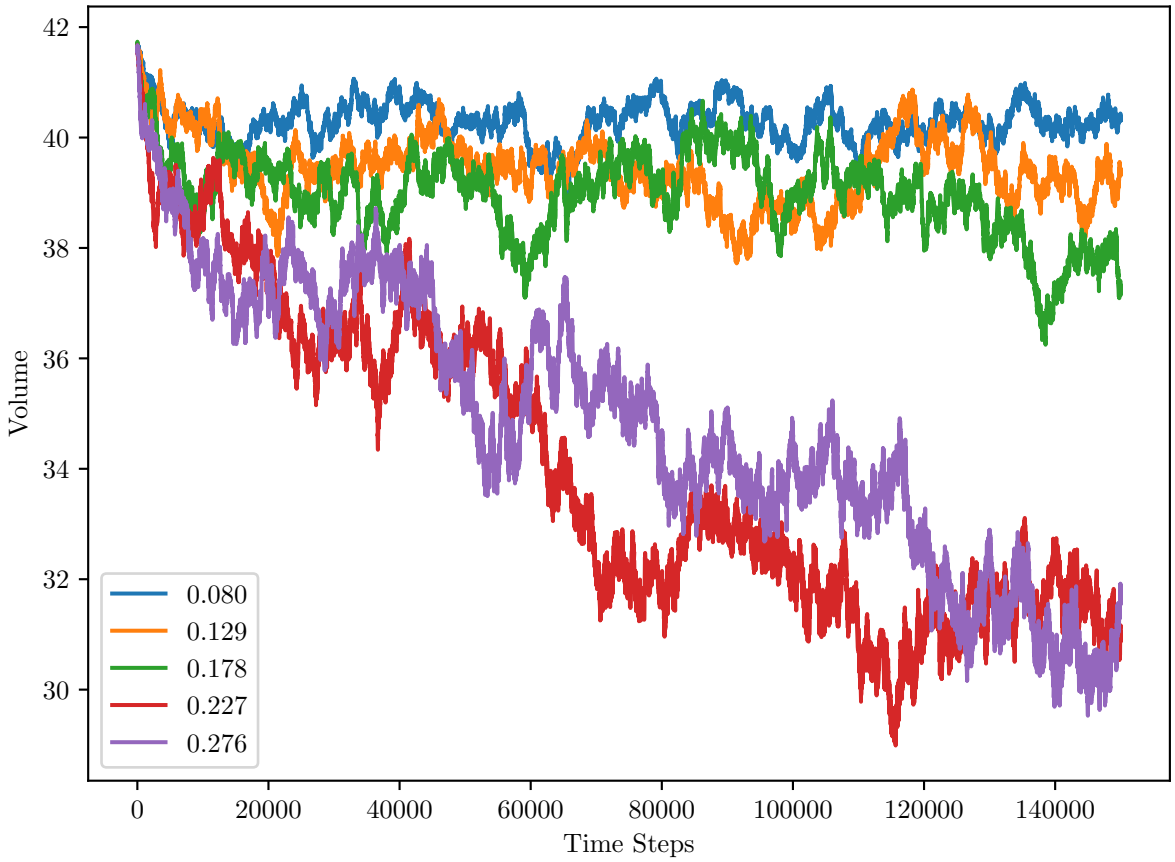

Figure 3.8: The volume of the shell as a function of time has a negative slope at temperatures above the crumpling temperature. The plots for $\gamma = 2541.1$ for increasing temperatures has been shown.

In next section we present the thermal response of $T = 7$ Caspar-Klug shell that has 72 particles as a function of FvK number for fixed α.

3.2.3 Phase Diagram

We heated up a $N = 72$ Caspar-Klug shell for 2×10^6 time steps for various combinations of γ and $1/\beta$ values. We determined the melting temperatures for γ values below the buckling transition. For γ values above the buckling transition we determined the crumpling temperature as per the discussion in Section 3.2.2. The results have been summarized in a phase diagram shown in Figure 3.10. The key observations are as follows.

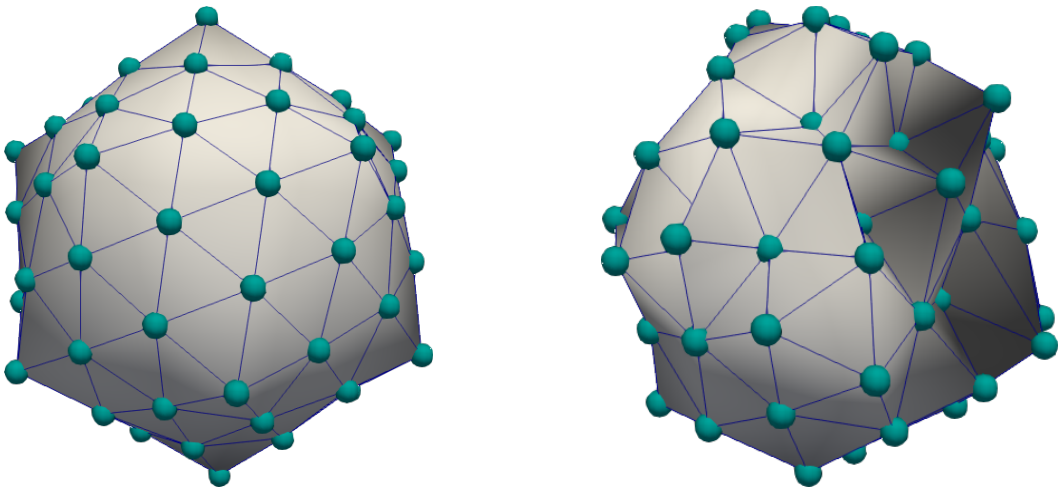

(a) t = 1 (b) t = 2000000

Figure 3.9: Visualization of oriented particles for $\gamma = 101344$ and $1/\beta = 0.079$ at different time steps t. As time progresses, the shell crumples. The edges have been shown only to highlight the crumpled structure.

1. Melting temperature decreases with increase in FvK number. Shells with higher FvK number have lower resistance to bending out of plane. The out-of-plane deformations aid melting.

2. Melting can be reliably detected only for FvK numbers lower than the buckling transition. For these structures, volume of the shell fluctuates about a steady state value even after long time. For FvK numbers larger than the buckling transition, increasing temperature causes a decrease in volume of the shell due to generation of effective thermal pressure [PVG12, KN17]. This leads the shell to become crumpled and the particles can no longer flow on the surface which prevents melting.

3. The melting behavior smoothly transitions into a crumpling behavior as we increase the FvK number across the buckling transition.

4. The theoretical prediction for crumpling temperature given by Equation 3.21 are much higher than the temperatures obtained in our simulations. This is because Equation 3.21 is applicable for a continuum model of a shell and requires a large number of

particles. There is mismatch because finite size effects are substantial.

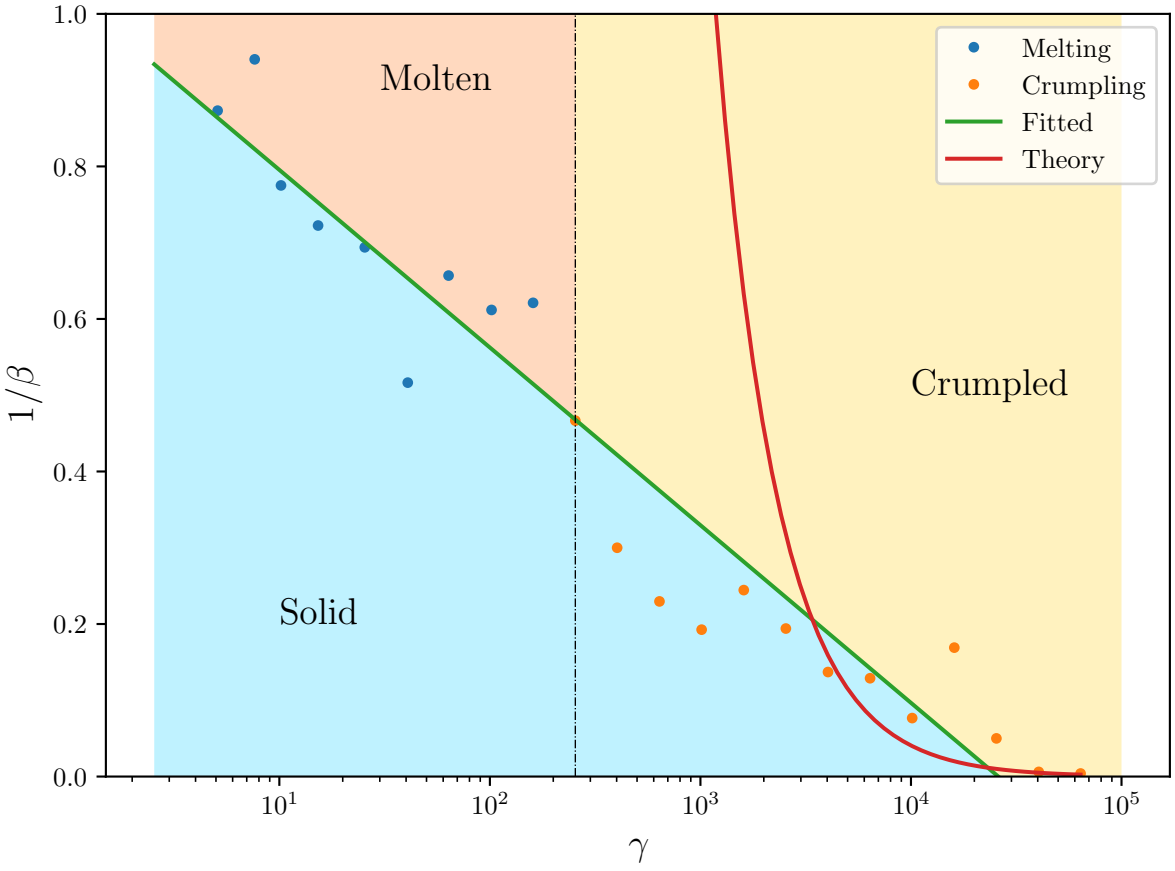

Figure 3.10: Thermal response of Caspar-Klug shell with $N = 72$ particles has been shown as a function of FvK number. The vertical dashed line marks the zero temperature buckling transition. For FvK numbers below the buckling transition the structure undergoes melting when heated. But for FvK numbers higher than the buckling transition, heating results into an effective external pressure which crumples the shell and thus precludes melting. Blue dots mark the melting temperatures. Orange dots indicate the onset of crumpling. Blue dots mark the melting temperatures. Orange dots indicate the onset of crumpling. Green line is a linear fit across the melting and crumpling points indicating that the two phenomenon have same slope on a semi-log plot. The red curve is a plot of Equation 3.21. The colored regions represent the three parts of the phase diagram where the structure is either in a solid phase or in a crumpled phase or in a molten phase.

CHAPTER 4

Conclusion and Future Work

4.1 Conclusion

We have explored the effect of discreteness on thermal and mechanical response of closed deformable shells made up of a small number of particles. Starting with the continuum elasticity model we introduced discreteness in two steps. In the first step we replaced the in-plane stretching energy with Morse potentials while retaining the Helfrich energy as it is. In the second step we replaced even the Helfrich bending energy with special oriented-particle potentials. Using the hybrid model we found that shells with icosahedral symmetry are stable only at large FvK numbers. For lower FvK numbers, for a narrow Morse potential, there is co-existence of structures with different symmetries but comparable energies. The difference in energies of these structures is of the order of energy of thermal fluctuations. Although the hybrid model predicts instability of icosahedral symmetry at low FvK numbers, experiments show the presence of spherical shells in viruses. Spherical shells imply low FvK numbers and icosahedral symmetry. So there may be additional mechanisms which provide stability for the icosahedral structure at low FvK numbers.

The fully discrete model showed that the buckling transition has a great significance even at finite temperature. It controls the thermal response of the shell. At low FvK numbers we can melt the shell by heating. But at high FvK numbers the shell crumples into a 3D cluster instead of melting due to generation of an effective external pressure.

4.2 Future Work

The phase diagram 3.10 shows considerable deviation of the theoretical crumpling temperature and the crumpling temperature observed in the simulations. The theoretical prediction is based on the work of Košmrlj *et al* [KN17] and it uses a continuum model. We hypothesized in Section 3.2.3 that finite size effects are responsible for the discrepancy. To test this hypothesis, we can repeat the simulations of Chapter 3 for increasing number of particles and observe whether the crumpling curve approaches the theoretical prediction in the phase diagram.

Atomic force microscopy is used to image microscopic structures and record their mechanical response. Many studies have reported on the use of this technique to investigate the material properties of viral capsids [ZHD17, CR13]. Certainly, the mechanical response of the viral capsids depends a lot on the nanoscale structural details of its constituent proteins and membranes. Nevertheless, coarse-grained models have been successfully used to explain some of the observed mechanical response of viral shells [KBM06]. It is known that viral capsids can have different behavior under different loading regimes. Under sufficiently high loads the shells can undergo plastic deformation. Sometimes, when the indenting force is removed, the shells gradually recover either partially or fully over a finite relaxation time. Thus they may have a viscoelastic behavior. Thermal fluctuations play a key role in this phenomenon. The discrete model includes viscosity. Therefore, studying the indentation behavior of capsids with this model is one natural extension of the current work.

APPENDIX A

Derivatives of OPS Potentials

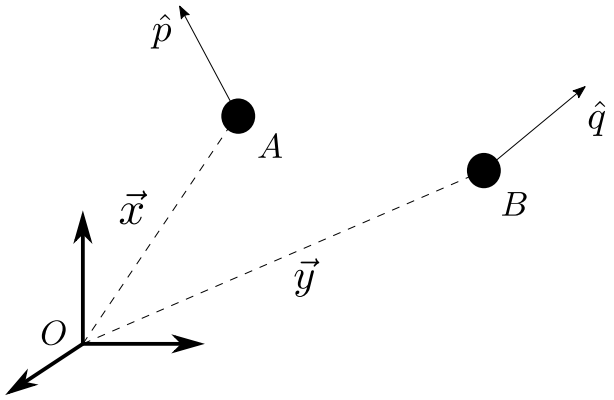

Figure A.1: Two oriented particles A and B having position vectors $\vec{\mathbf{x}}$ and $\vec{\mathbf{y}}$, respectively, with respect to origin O. Their orientations are unit vectors $\hat{\mathbf{p}}$ and $\hat{\mathbf{q}}$, respectively.

Consider two oriented particles A and B as shown in Figure A.1. Their position vectors are $\vec{\mathbf{x}}$ and $\vec{\mathbf{y}}$ respectively. Their orientations are represented by unit vectors $\hat{\mathbf{p}}$ and $\hat{\mathbf{q}}$, respectively. The orientations unit vectors are themselves functions of rotation vectors $\vec{\mathbf{u}}$ and $\vec{\mathbf{v}}$ respectively. Let

$$\vec{\mathbf{r}} = \vec{\mathbf{y}} - \vec{\mathbf{x}}$$

$$r = ||\vec{\mathbf{r}}||$$

$$\hat{\mathbf{r}} = \frac{\vec{\mathbf{r}}}{r}$$

The energy of oriented particle systems (OPS) is calculated as

$$E = \phi_M(r) + \frac{K}{V_M}\left(\phi_N(\hat{\mathbf{p}}, \hat{\mathbf{q}}) + \phi_P(\hat{\mathbf{p}}, \hat{\mathbf{q}}, \hat{\mathbf{r}}) + \phi_C(\hat{\mathbf{p}}, \hat{\mathbf{q}}, \hat{\mathbf{r}})\ \right). \tag{A.1}$$

ϕ_M is the Morse potential with parameters a and r_e

$$\phi_M = e^{-2a(r-r_e)} - 2e^{-a(r-r_e)}. \tag{A.2}$$

The co-circularity potential, ϕ_P, is

$$\phi_P = \left(\frac{\hat{\mathbf{p}} \cdot \hat{\mathbf{r}}}{r}\right)^2. \tag{A.3}$$

The co-normality potential, ϕ_N, is

$$\phi_N = ||\hat{\mathbf{p}} - \hat{\mathbf{q}}||^2. \tag{A.4}$$

The co-circularity potential, ϕ_C, is

$$\phi_C = \left((\hat{\mathbf{p}} + \hat{\mathbf{q}}) \cdot \frac{\hat{\mathbf{r}}}{r}\right)^2. \tag{A.5}$$

A.1 Derivatives of Morse Potential

Taking derivatives of equation A.2 with respect to x_j and y_j we get

$$\frac{\partial \phi_M}{\partial x_j} = -\frac{2ar_j}{r}\left(e^{-a(r-r_e)} - e^{-2a(r-r_e)}\right) \tag{A.6}$$

$$\frac{\partial \phi_M}{\partial y_j} = \frac{2ar_j}{r}\left(e^{-a(r-r_e)} - e^{-2a(r-r_e)}\right). \tag{A.7}$$

A.2 Derivatives of Orientations

The orientations $\hat{\mathbf{p}}$ and $\hat{\mathbf{q}}$ can be obtained by rotating the global z-axis $\hat{\mathbf{e_z}}$ by rotation vectors $\vec{\mathbf{u}}$ and $\vec{\mathbf{v}}$ respectively. Let u_i and v_i (with $i = 0, 1, 2$) represent components of the rotation vector and

$$u = ||\vec{\mathbf{u}}||$$

$$v = ||\vec{\mathbf{v}}||.$$

The angle of rotations are then given by

$$\alpha = \frac{u}{2}$$

$$\beta = \frac{v}{2}.$$

The components of $\hat{\mathbf{p}}$ are

$$p_0 = \frac{2\sin\alpha}{u^2}\left(u_1 u\cos\alpha + u_0 u_2 \sin\alpha\right) \tag{A.8}$$

$$p_1 = \frac{2\sin\alpha}{u^2}\left(-u_0 u\cos\alpha + u_1 u_2 \sin\alpha\right) \tag{A.9}$$

$$p_2 = \cos^2\alpha + \frac{\sin^2\alpha}{u^2}\left(u_2^2 - u_1^2 - u_0^2\right). \tag{A.10}$$

While calculating derivatives of $\hat{\mathbf{p}}$ and $\hat{\mathbf{q}}$ with respect to components of $\vec{\mathbf{u}}$ and $\vec{\mathbf{v}}$, care must be taken that α and β are also functions of the components of $\vec{\mathbf{u}}$ and $\vec{\mathbf{v}}$, respectively.

Let's denote the derivatives of components of orientations with respect to components of rotation vectors as

$$M_{ij} = \frac{\partial p_j}{\partial u_i} \tag{A.11}$$

$$N_{ij} = \frac{\partial q_j}{\partial v_i}, \tag{A.12}$$

where $i, j = 0, 1, 2$. The quaternion representing the z-axis is

$$Z = (0, 0, 0, 1)$$

The quaternion representing the rotation by rotation vector $\hat{\mathbf{p}}$ is

$$\begin{aligned} Q &= (q_0, q_1, q_2, q_3) \\ &= \left(\cos\alpha, \frac{u_0}{u}\sin\alpha, \frac{u_1}{u}\sin\alpha, \frac{u_2}{u}\sin\alpha\right) \end{aligned}$$

The relationship between $\hat{\mathbf{p}}, Q$ and Z is

$$\hat{\mathbf{p}} = Q * Z * Q^T$$

where $*$ represents *Hamilton* product. We can calculate M_{ij} as

$$M_{ij} = \frac{\partial p_j}{\partial Q_a}\frac{\partial Q_a}{\partial u_i}$$

where $a = 0, 1, 2, 3$ and $i, j = 1, 2, 3$. Let

$$A_{aj} = \frac{\partial p_j}{\partial Q_a} \qquad B_{ia} = \frac{\partial Q_a}{\partial u_i}$$

where A is a 4×3 matrix and B is a 3×4 matrix. Therefore,

$$M_{ij} = B_{ia} A_{aj}$$

It can be shown that

$$A_{aj} = \frac{\partial p_j}{\partial Q_a} = 2 \times \begin{bmatrix} q_2 & -q_1 & q_0 \\ q_3 & -q_0 & -q_1 \\ q_0 & q_3 & -q_2 \\ q_1 & q_2 & q_3 \end{bmatrix} \tag{A.13}$$

Now let's look at how to calculate $\frac{\partial Q_a}{\partial u_i}$. First we will differentiate only Q_0. This will give us the first *column* of the 3×4 matrix $\frac{\partial Q_a}{\partial u_i}$.

$$B_{i0} = \frac{\partial Q_0}{\partial u_i} = -\frac{\sin \alpha}{2u} u_i \tag{A.14}$$

The remaining three components of Q_a give us the remaining 3 *columns*,

$$B_{ij} = \frac{\partial Q_j}{\partial u_i} = \frac{\sin \alpha}{u} \delta_{ij} + \left(\frac{\cos \alpha}{2u^2} - \frac{\sin \alpha}{u^3} \right) u_i u_j \tag{A.15}$$

This equation will give a 3×3 matrix. We will stack this matrix to the right of the column vector obtained from $\frac{\partial Q_0}{\partial u_i}$ to get the full 3×4 matrix.

A.3 Derivatives of Co-Planarity Potential

The co-planarity potential (equation A.3) can be written in index notation as

$$\phi_p = \left(\frac{p_i r_i}{r} \right)^2, \tag{A.16}$$

where $r_i = y_i - x_i$. Differentiating with respect to x_j and y_j, we get

$$\frac{\partial \phi_P}{\partial x_j} = \frac{2 p_i r_i}{r^4} \left((p_i r_i)\, r_j - r^2 p_j \right) \tag{A.17}$$

$$\frac{\partial \phi_P}{\partial y_j} = \frac{2 p_i r_i}{r^4} \left(r^2 p_j - (p_i r_i)\, r_j \right) \tag{A.18}$$

For derivatives with respect to u_j, we can use chain rule as

$$\frac{\partial \phi_P}{\partial u_i} = \frac{\partial \phi_P}{\partial p_k} \frac{\partial p_k}{\partial u_i} = \frac{2 p_j r_j}{r^2} M_{ik} r_k \tag{A.19}$$

A.4 Derivatives of Co-Normality Potential

We can write the co-normality potential (equation A.4) as

$$\phi_N = p_i p_i + q_i q_i - 2 p_i q_i,$$

where $i = 0, 1, 2$ and summation is implied over repeated indices. Therefore, differentiating with respect to p_j and q_j gives,

$$\frac{\partial \phi_N}{\partial p_j} = 2\left(p_j - q_j\right) \tag{A.20}$$

$$\frac{\partial \phi_N}{\partial q_j} = -2\left(p_j - q_j\right) \tag{A.21}$$

Therefore, derivatives of ϕ_N with respect to u_i and v_i are

$$\frac{\partial \phi_N}{\partial u_i} = \frac{\partial \phi_N}{\partial p_j}\frac{\partial p_j}{\partial u_i} \tag{A.22}$$

$$\frac{\partial \phi_N}{\partial v_i} = \frac{\partial \phi_N}{\partial q_j}\frac{\partial q_j}{\partial v_i} \tag{A.23}$$

If we let $m_j = p_j - q_j$ then we can write the above equations concisely as,

$$\frac{\partial \phi_N}{\partial u_i} = 2 M_{ij} m_j \tag{A.24}$$

$$\frac{\partial \phi_N}{\partial v_i} = -2 N_{ij} m_j \tag{A.25}$$

A.5 Derivatives of Co-circularity Potential

If we let

$$n_i = p_i + q_i$$

$$r_i = y_i - x_i,$$

then we can write the co-circularity potential (equation A.5) as

$$\phi_c = \left(\frac{n_i r_i}{r}\right)^2$$

Differentiating with respect to x_j and y_j, we get

$$\frac{\partial \phi_C}{\partial x_j} = \frac{2n_i r_i}{r^4}\left(\left(n_i r_i\right) r_j - r^2 n_j\right) \tag{A.26}$$

$$\frac{\partial \phi_C}{\partial y_j} = \frac{2n_i r_i}{r^4}\left(r^2 n_j - \left(n_i r_i\right) r_j\right) \tag{A.27}$$

To differentiate ϕ_C with respect to p_k and q_k we can write it as

$$\phi_C = \left(\frac{\left(p_i + q_i\right) r_i}{r}\right)^2$$

Therefore, we get

$$\frac{\partial \phi_C}{\partial p_k} = \frac{\partial \phi_C}{\partial q_k} = \frac{2n_i r_i}{r^2} r_k \tag{A.28}$$

We can use chain rule to differentiate ϕ_C with respect to u_i and v_i.

$$\frac{\partial \phi_C}{\partial u_i} = \frac{\partial \phi_C}{\partial p_k}\frac{\partial p_k}{\partial u_i} = \frac{2n_j r_j}{r^2} M_{ik} r_k \tag{A.29}$$

$$\frac{\partial \phi_C}{\partial v_i} = \frac{\partial \phi_C}{\partial q_k}\frac{\partial q_k}{\partial v_i} = \frac{2n_j r_j}{r^2} N_{ik} r_k \tag{A.30}$$

A.6 Derivatives of Total Energy

The most crucial part of the code implementation is to calculate the matrices M_{ij} and N_{ij} carefully.

$$\frac{\partial E}{\partial x_j} = \frac{\partial \phi_M}{\partial x_j} + \frac{K}{V_M}\frac{\partial \phi_C}{\partial x_j} \tag{A.31}$$

$$\frac{\partial E}{\partial y_j} = -\frac{\partial E}{\partial x_j} \tag{A.32}$$

$$\frac{\partial E}{\partial u_j} = \frac{K}{V_M}\left(\frac{\partial \phi_N}{\partial u_j} + \frac{\partial \phi_C}{\partial u_j}\right) \tag{A.33}$$

$$\frac{\partial E}{\partial v_j} = \frac{K}{V_M}\left(\frac{\partial \phi_N}{\partial v_j} + \frac{\partial \phi_C}{\partial v_j}\right) \tag{A.34}$$

APPENDIX B

Notes on Computer Implementation

B.1 Hybrid Model

The computer program used for simulations presented in Chapter 2 is part of `voom` package which is hosted at `https://github.com/wsklug/voom`. The package is written in `C++`. The driver code is in the `asphericityMorse.cc` file located at `https://github.com/wsklug/voom/blob/master/src/Applications/Capsid/asphericityMorse.cc`. Understanding the code requires familiarity with Finite Element Method. We will give a brief overview of the code organization next.

The driver reads an input file containing the starting configuration of the hybrid model shell from a `.vtk` file. This file contains information about point coordinates and their connectivity to form a mesh. The Visualization Tool Kit library is used in `voom` to read and write `.vtk` files. The code also reads a sequence of FvK numbers from a file named `fvkSteps.dat` present in the same directory as the program. For every FvK number we solve for the minimum energy configuration of the shell as obtained from an optimization routine and write out the asphericity and other quantities worth monitoring to an output file. The code also saves the particle positions for the minimum energy state in a `.vtk` file. The input FvK numbers are arranged in increasing or decreasing order and the solution from the previous FvK number is used as the initial guess for the solution at the next FvK number. The code has provision to do some pre-processing on the input mesh. It rescales the mesh so that each edge has unit length. It can optionally project the input points to a sphere. There is also provision to relax the particle positions using harmonic springs to ensure that all edges are of equal length. Option flags and input parameters are supplied through a miscellaneous

input data file named `miscInp.dat` which should be present in the same directory as the program executable. The code can also remesh the shell if after energy minimization any of the triangles of the mesh have aspect ratio higher than an input tolerance value. The remeshing is done by flipping edges among adjacent triangles. The tolerance limit for the aspect ratio can be set using `miscInp.dat` input file.

The driver uses an object of `Solver` class to perform the optimization. In our case, we will use a `C++` wrapper to the LBFGS [ZBL97] solver available in `voom`. A `Solver` object stores a reference to an object of `Model` class. A `Model` represents a collection of objects of `Body` class. A `Body` represents a set of finite elements. It contains information about the shape functions of the finite elements. The material properties of the finite elements are supplied as an input to the constructor of the `Body` object. In our case, we use two child classes of `Body` class — `LoopShellBody` and `PotentialBody`. `LoopShellBody` represents the surface of the hybrid model discretized using Loop subdivision shell [COS00] finite elements. The implementation is based on the work by Feng and Klug [FK06]. `PotentialBody` is used to model the Morse interactions between vertices of the finite element mesh corresponding to the `LoopShellBody`. Each child class of `Body` implements a `compute()` method which calculates energy and its Jacobian with respect to the degrees of freedom associated with all its finite elements. The `Model` object performs *assembly* of the energy and the Jacobians calculated by the set of `Body` objects it contains. *Assembly* is a standard step in finite element analysis.

The `Solver` solves for the positions of the particles forming the hybrid model shell, iteratively. At every iteration it calculates the current value for the position coordinates and asks `Model` to provide energy and Jacobian for these values. The `Model` iterates over each `Body` object that it stores for these calculations. The optimization loop terminates based on various configurable criteria like when change in norm of solution vector reaches close to machine precision etc.

B.2 OPS Model

The code used for simulations presented in Chapter 3 have been made available publicly on `https://github.com/amit112amit/oriented-particles`. This is a `C++` package. This package also follows the `Model` and `Solver` format of code organization like for the hybrid model as explained in Section B.1. The main driver used for the simulations discussed in Chapter 3 is `HeatOPSModel.cxx` located at `https://github.com/amit112amit/oriented-particles/blob/master/src/Drivers/HeatOPSModel.cxx`

The simulations reported in Chapter 3 were run for one to two million time steps. These simulations were run on Hoffman2 cluster as batch jobs. We had facility to run simulations with a run time of 24 hours in one go. Sometimes this was not sufficient to complete all the timesteps required. Therefore, the code has provision to save its state periodically so that if the simulation does not complete within 24 hours we can resume the simulation from the last saved state in another batch job. The driver first checks for an existing state file in the working directory to determine if it needs to resume an incomplete simulation or start a new one. A state file stores the position and orientational degrees of freedom, the state of random number generator for the Brownian forces and the input parameters. If a state file is not found, these values are initialized to default values or read from input files. There are two input files. One input file is provided using a command line argument. It contains the coordinates of vertices of a Caspar Klug structure. These coordinates are used to calculate the orientations. The second input file must have name `schedule.dat` and must be present in the working directory. It consists of a combination of temperature and FvK numbers and the number of time steps for which the simulation has to be run for each combination.

For each time step, we generate Brownian forces for each particle of the shell. Then we solve the Augmented Lagrangian problem to solve Equation 3.14. The Brownian forces may result in rigid body motion of the shell. We use Kabsch algorithm [Kab76] to cancel the rigid body motion. Output of the Kabsch algorithm is the final solution of the time step. Periodically, we print out a `.vtk` file containing particle positions and orientations. We also save a state file to facilitate resuming the simulation. The frequency of saving these files can

be controlled using `schedule.dat` input file. We calculate the mean-squared displacement, volume and asphericity at every time step and write it to an output file.

REFERENCES

[AB76] KW Adolph and PJG Butler. "Assembly of a spherical plant virus." *Phil. Trans. R. Soc. Lond. B*, **276**(943):113–122, 1976.

[Agg18] Ankush Aggarwal. "Determination of prestress and elastic properties of virus capsids." *Physical Review E*, **97**(3):032414, 2018.

[ARW09] Anton Arkhipov, Wouter H Roos, Gijs JL Wuite, and Klaus Schulten. "Elucidating the mechanism behind irreversible deformation of viral capsids." *Biophysical journal*, **97**(7):2061–2069, 2009.

[BBW69] JB Bancroft, CE Bracker, and GW Wagner. "Structures derived from cowpea chlorotic mottle and brome mosaic virus protein." *Virology*, **38**(2):324–335, 1969.

[BDT16] Arthur Bousquet, Bogdan Dragnea, Manel Tayachi, and Roger Temam. "Towards the modeling of nanoindentation of virus shells: Do substrate adhesion and geometry matter?" *Physica D: Nonlinear Phenomena*, **336**:28–38, 2016.

[BGL85] V.M. Bedanov, G.V. Gadiyak, and Yu.E. Lozovik. "On a modified Lindemann-like criterion for 2D melting." *Physics Letters A*, **109**(6):289 – 291, 1985.

[BGR03] Robijn F Bruinsma, William M Gelbart, David Reguera, Joseph Rudnick, and Roya Zandi. "Viral self-assembly as a thermodynamic process." *Physical review letters*, **90**(24):248101, 2003.

[BOF99] TS Baker, NH Olson, and SD Fuller. "Adding the third dimension to virus life cycles: three-dimensional reconstruction of icosahedral viruses from cryo-electron micrographs." *Microbiology and Molecular Biology Reviews*, **63**(4):862–922, 1999.

[CK62] Donald L D Caspar and Aaron Klug. "Physical principles in the construction of regular viruses." In *Cold Spring Harbor symposia on quantitative biology*, volume 27, pp. 1–24. Cold Spring Harbor Laboratory Press, 1962.

[COS00] Fehmi Cirak, Michael Ortiz, and Peter Schröder. "Subdivision surfaces: a new paradigm for thin-shell finite-element analysis." *International Journal for Numerical Methods in Engineering*, **47**(12):2039–2072, 2000.

[CR13] Marek Cieplak and Mark O. Robbins. "Nanoindentation of 35 Virus Capsids in a Molecular Model: Relating Mechanical Properties to Structure." *PLoS ONE*, **8**(6), 2013.

[CSB09] Mauricio Carrillo-Tripp, Craig M. Shepherd, Ian A. Borelli, Sangita Venkataraman, Gabriel Lander, Padmaja Natarajan, John E. Johnson, Charles L. Brooks, III, and Vijay S. Reddy. "VIPERdb2: an enhanced and web API enabled relational database for structural virology." *Nucleic Acids Research*, **37**(suppl_1):D436–D442, 2009.

[CW56] F. H.C. Crick and J. D. Watson. "Structure of small viruses." *Nature*, **177**(4506):473–475, 1956.

[CZ02] Pablo Ceres and Adam Zlotnick. "Weak protein- protein interactions are sufficient to drive assembly of hepatitis B virus capsids." *Biochemistry*, **41**(39):11525–11531, 2002.

[EM78] Donald L Ermak and JA McCammon. "Brownian dynamics with hydrodynamic interactions." *The Journal of chemical physics*, **69**(4):1352–1360, 1978.

[FCW10] Szilard N Fejer, Dwaipayan Chakrabarti, and David J Wales. "Emergent complexity from simple anisotropic building blocks: shells, tubes, and spirals." *ACS nano*, **4**(1):219–228, 2010.

[FER04] SJ Flint, LW Enquist, VR Racaniello, and AM Skalka. "Principles of Virology.", 2004.

[FK59] JT Finch, A Klug, et al. "Structure of PoliomyelitisVirus." *Nature*, **183**:1709–14, 1959.

[FK06] Feng Feng and William S Klug. "Finite element modeling of lipid bilayer membranes." *Journal of Computational Physics*, **220**(1):394–408, 2006.

[GKH18] Rodrigo E Guerra, Colm P Kelleher, Andrew D Hollingsworth, and Paul M Chaikin. "Freezing on a sphere." *Nature*, **554**(7692):346, 2018.

[GLK99] Barbie K Ganser, Su Li, Victor Y Klishko, John T Finch, and Wesley I Sundquist. "Assembly and analysis of conical models for the HIV-1 core." *Science*, **283**(5398):80–83, 1999.

[HBW08] J Bernard Heymann, Carmen Butan, Dennis C Winkler, Rebecca C Craven, and Alasdair C Steven. "Irregular and semi-regular polyhedral models for Rous sarcoma virus cores." *Computational and mathematical methods in medicine*, **9**(3-4):197–210, 2008.

[Kab76] W. Kabsch. "A solution for the best rotation to relate two sets of vectors." *Acta Crystallographica Section A*, **32**(5):922–923, Sep 1976.

[KBM06] William S Klug, Robijn F Bruinsma, Jean Philippe Michel, Charles M Knobler, Irena L Ivanovska, Christoph F Schmidt, and Gijs J L Wuite. "Failure of viral shells." *Physical Review Letters*, **97**(22):1–4, 2006.

[KM10] Kristopher J. Koudelka and Marianne Manchester. *The Use of Viruses in Biomedical Nanotechnology*. Imperial College Press, London, 2010.

[KN17] Andrej Košmrlj and David R Nelson. "Statistical mechanics of thin spherical shells." *Physical Review X*, **7**(1):011002, 2017.

[KRW12] W. S. Klug, W. H. Roos, and G. J.L. Wuite. "Unlocking internal prestress from protein nanoshells." *Physical Review Letters*, **109**(16):1–5, 2012.

[LGP09] L Lavelle, M Gingery, M Phillips, WM Gelbart, CM Knobler, RD Cadena-Nava, JR Vega-Acosta, LA Pinedo-Torres, and J Ruiz-Garcia. "Phase diagram of self-assembled viral capsid protein polymorphs." *The Journal of Physical Chemistry B*, **113**(12):3813–3819, 2009.

[LMN03] Jack Lidmar, Leonid Mirny, and David R Nelson. "Virus shapes and buckling transitions in spherical shells." *Physical review. E, Statistical, nonlinear, and soft matter physics*, **68**:051910, 2003.

[LZR10] Antoni Luque, Roya Zandi, and David Reguera. "Optimal architectures of elongated viruses." *Proceedings of the National Academy of Sciences*, **107**(12):5323–5328, 2010.

[MRB10] A Morozov, J Rudnick, R Bruinsma, and W Klug. *Emerging Topics in Physical Virology, eds P Stockley and R Twarock*. Imperial College Press, London, 2010.

[OPP14] Angelo Onofrio, Giovanni Parisi, Giuseppe Punzi, Simona Todisco, Maria Antonietta Di Noia, Fabrizio Bossis, Antonio Turi, Anna De Grassi, and Ciro Leonardo Pierri. "Distance-dependent hydrophobic–hydrophobic contacts in protein folding simulations." *Physical Chemistry Chemical Physics*, **16**(35):18907–18917, 2014.

[PKW16] Stefan Paquay, Halim Kusumaatmaja, David J. Wales, Roya Zandi, and Paul van der Schoot. "Energetically favoured defects in dense packings of particles on spherical surfaces." *Soft Matter*, **12**(1):1–25, 2016.

[PM98] A. Pérez-Garrido and MA Moore. "Simulations of two-dimensional melting on the surface of a sphere." *Physical Review B*, **58**(15):9677, 1998.

[PVG12] Jayson Paulose, Gerard A Vliegenthart, Gerhard Gompper, and David R Nelson. "Fluctuating shells under pressure." *Proceedings of the National Academy of Sciences of the United States of America*, **109**(48):19551–6, 2012.

[RBW10] W. Roos, R. Bruinsma, and G. Wuite. "Physical virology." *Nat Phys*, **6**(10):733–743, 2010.

[SEN11] Peter S Shen, Dirk Enderlein, Christian DS Nelson, Weston S Carter, Masaaki Kawano, Li Xing, Robert D Swenson, Norman H Olson, Timothy S Baker, R Holland Cheng, et al. "The structure of avian polyomavirus reveals variably sized capsids, non-conserved inter-capsomere interactions, and a possible location of the minor capsid protein VP4." *Virology*, **411**(1):142–152, 2011.

[SN88] H. S. Seung and David R. Nelson. "Defects in flexible membranes with crystalline order." *Physical Review A*, **38**(2):1005–1018, 1988.

[SPB17] Amit R Singh, Luigi E Perotti, Robijn F Bruinsma, Joseph Rudnick, and William S Klug. "Ground state instabilities of protein shells are eliminated by buckling." *Soft matter*, **13**(44):8300–8308, 2017.

[ST92] Richard Szeliski and David Tonnesen. *Surface modeling with oriented particle systems*, volume 26. ACM, 1992.

[Vor08] Georges Voronoi. "Nouvelles applications des paramètres continus à la théorie des formes quadratiques. Deuxième mémoire. Recherches sur les parallélloèdres primitifs." *Journal für die reine und angewandte Mathematik*, **134**:198–287, 1908.

[Wei] Eric W. Weisstein. "Polyhedral Formula." http://mathworld.wolfram.com/PolyhedralFormula.html. Accessed: 2018-09-13.

[WOB12] Ruijin Wu, Aysegul Ozkan, Antonette Bennett, Mavis Agbandje-Mckenna, and Meera Sitharam. "Robustness measure for an adeno-associated viral shell self-assembly is accurately predicted by configuration space atlasing using EASAL." In *Proceedings of the ACM Conference on Bioinformatics, Computational Biology and Biomedicine*, pp. 690–695. ACM, 2012.

[WS58] Robley C Williams and Kenneth M Smith. "The polyhedral form of the Tipula iridescent virus." *Biochimica et biophysica acta*, **28**:464–469, 1958.

[YJJ17] Xuekui Yu, Jonathan Jih, Jiansen Jiang, and Z Hong Zhou. "Atomic structure of the human cytomegalovirus capsid with its securing tegument layer of pp150." *Science*, **356**(6345):eaam6892, 2017.

[ZBL97] Ciyou Zhu, Richard H Byrd, Peihuang Lu, and Jorge Nocedal. "Algorithm 778: L-BFGS-B: Fortran subroutines for large-scale bound-constrained optimization." *ACM Transactions on Mathematical Software (TOMS)*, **23**(4):550–560, 1997.

[ZHD17] Cheng Zeng, Mercedes Hernando-Pérez, Bogdan Dragnea, Xiang Ma, Paul Van Der Schoot, and Roya Zandi. "Contact Mechanics of a Small Icosahedral Virus." *Physical Review Letters*, **119**(3):1–6, 2017.

[Zlo03] Adam Zlotnick. "Are weak protein–protein interactions the general rule in capsid assembly?" *Virology*, **315**(2):269–274, 2003.

[ZR05] Roya Zandi and David Reguera. "Mechanical properties of viral capsids." *Physical Review E - Statistical, Nonlinear, and Soft Matter Physics*, **72**(2):1–12, 2005.

[ZRB04] Roya Zandi, David Reguera, Robijn F Bruinsma, William M Gelbart, and Joseph Rudnick. "Origin of icosahedral symmetry in viruses." *Proceedings of the National Academy of Sciences of the United States of America*, **101**(44):15556–60, 2004.